Light Ion Beam Fusion Target Development Facility Studies: Progress Report for the Period November 1, 1986 to October 31, 1987

B. Badger, D. Bruggink, R.L. Engelstad, D.L. Henderson, E.G. Lovell, G.A. Moses, R.R. Peterson, M.E. Sawan, O. Yasar

January 1988

UWFDM-752

FUSION TECHNOLOGY INSTITUTE

UNIVERSITY OF WISCONSIN

MADISON WISCONSIN

DISCLAIMER

This report was prepared as an account of work sponsored by an agency of the United States Government. Neither the United States Government, nor any agency thereof, nor any of their employees, makes any warranty, express or implied, or assumes any legal liability or responsibility for the accuracy, completeness, or usefulness of any information, apparatus, product, or process disclosed, or represents that its use would not infringe privately owned rights. Reference herein to any specific commercial product, process, or service by trade name, trademark, manufacturer, or otherwise, does not necessarily constitute or imply its endorsement, recommendation, or favoring by the United States Government or any agency thereof. The views and opinions of authors expressed herein do not necessarily state or reflect those of the United States Government or any agency thereof.

Light Ion Beam Fusion Target Development Facility Studies: Progress Report for the Period November 1, 1986 to October 31, 1987

B. Badger, D. Bruggink, R.L. Engelstad, D.L. Henderson, E.G. Lovell, G.A. Moses, R.R. Peterson, M.E. Sawan, O. Yasar

Fusion Technology Institute
University of Wisconsin
1500 Engineering Drive
Madison, WI 53706

http://fti.neep.wisc.edu

January 1988

UWFDM-752

LIGHT ION BEAM FUSION TARGET DEVELOPMENT FACILITY STUDIES: PROGRESS REPORT FOR THE PERIOD 1 NOVEMBER 1986 TO 31 OCTOBER 1987

B. Badger, D. Bruggink, R.L. Engelstad, D.L. Henderson,

E.G. Lovell, G.A. Moses, R.R. Peterson, M.E. Sawan, O. Yasar

Fusion Technology Institute
University of Wisconsin-Madison
1500 Johnson Drive
Madison, WI 53706

January 1988

UWFDM-752

1. INTRODUCTION

1.1 Statement of Work and Summary of Results

During the period from October 1986 to October 1987 we have addressed three general technical areas associated with the design of the Light Ion Fusion Target Development Facility (TDF). These are: (1) mechanical analysis of the target chamber, (2) activation analysis of the target chamber and diodes, and (3) plasma channel formation and ion propagation. Much of this work has been part of a design of a one meter radius target chamber. The specific statement of work is given in Table 1.1. The remainder of Chapter 1 is a summary of our results.

Chapter 2 contains a description of the neutron transport and activation calculations done for the one meter and three meter target chamber designs and for the diode in each of these cases. Improvements over earlier calculations include a more consistent geometrical model of the three meter design with the graphite moderator, a sensitivity study of the effectiveness of our 2-D approximation to the diode and the wall penetration and improved cross sections. Attention is also given to the discrete ordinates approximation of neutron streaming in the long narrow penetration through the wall and moderator. Different shield materials are put between the target chamber and diode in the one meter design to evaluate their effectiveness.

Chapter 3 contains a description of a finite element analysis of the three meter target chamber and a comparison to analytical results. Details such as penetrations have been included in the finite element analysis. This analysis shows that analytic results are reproduced for a simple uniform loading on an axisymmetric chamber and that the penetrations are small enough that their associated stress concentrations are adequately modelled as a penetration in an infinite plate. These results serve as a starting point for a detailed finite element design of the target chamber.

Chapter 4 is a discussion of plasma channel formation for the one meter design. Calculations of channel dynamics using the ZPINCH code indicate that the required magnetic field of 28 kG at a channel radius of 0.5 cm is difficult to achieve. The radiative properties of the channel play an important role in the dynamics.

Chapter 5 is a discussion of beam overlap at the target. The ION code has been used to model the ion trajectories in the overlap region near the target. For ideal plasma channel parameters the final transport efficiency through the overlap region is 70-80% depending upon the geometrical arrangement of the channels around the target. The lower efficiency comes with all channels on the same plane, while two layers of channels lead to a higher efficiency.

Table 1.1. Statement of Work

1. Supply a conceptual design of a disposable TDF target chamber of spherical shape and small radius (~ 1 m). This chamber shall contain the target blast and activated debris and shall be replaced after approximately 50 to 200 shots. The conceptual design shall consider the relevant lifetime limitations due to the effects of structural overpressure response, liner vaporization, liner shock response, etc. Calculations of neutron activation and time-dependent, after-shutdown dose rates shall be included in this task.

2. Modify the existing conceptual design of a three meter radius, cylindrical TDF target chamber to conform with graphite liner neutron activation reducing concepts. Calculations of neutron activation and time-dependent, after-shutdown dose rates shall be included in this task.

3. For the case of beamline penetrations and diagnostic and target injection ports for both spherical and cylindrical chamber designs, provide a comparison between a finite element structural analysis and modal structural analysis.

4. Utilize the CAD facility at U.W. for a collaborative (with SNL) integration of TDF pulsed power, diodes, target chamber, etc. into a full conceptual design.

5. Utilize the ION, ZPINCH and WINDOW computer codes in a study of ion beam propagation in the TDF channel overlap region. Provide an estimate of on-target power multiplication as a function of the number of plasma channels.

6. Utilize the ION, ZPINCH and WINDOW computer codes in a study of plasma channels for the one meter radius target chamber design. Provide estimates of the channel radius and current constraints for the wall confined or stabilized z-pinch portion of the channels.

Chapter 6 is a summary of the one meter target chamber design for TDF. At this stage, the one meter design has been completed to the same level of detail as the three meter design. Each is shown to be feasible. The major distinction between the two is the much lower activation of the three meter design. This comes with the additional design complications of a half meter thick graphite moderator region inside of the target chamber.

1.2 Publications

Publications are one way of measuring the productivity of research projects such as this one. Table 1.2 is a list of publications supported by the research project. Three papers were prepared for the 12th Symposium on Fusion Engineering and one refereed journal article was published.

1.3 Graduating Students

Roxann Engelstad, supported in part by this contract, graduated. She is currently employed with the Fusion Technology Institute at Wisconsin.

2. NEUTRONICS AND ACTIVATION

2.1. Introduction

The preliminary design of TDF uses aluminum 6061-T6 as the chamber wall material and has the target explosion chamber submerged in a borated water pool as portrayed in Fig. 2.1a. As an alternative to this three meter radius chamber design, a one meter radius chamber with two different first wall materials -- Al-6061-T6 and 2-1/4 Cr-1 Mo steel -- is examined. This is shown in Fig. 2.1b. The biological dose rates behind the first wall are compared for these wall materials. The three meter chamber design is also examined with a few changes from our previous studies.[1] In particular, the boron in the borated water pool surrounding the chamber is enriched to 90% boron-10 for neutron absorbing purposes. Also the 100 cm thick graphite moderator (40% void fraction) is replaced by 49 cm of graphite (no void). The dose rate at one week after shutdown behind the wall is increased from 25 mrem/hr[1] to 35 mrem/hr due to less graphite.

As a critical part of the TDF design, the high voltage diodes, which convert the electrical pulse into beams, are subject to neutron activation that can lead to high dose levels in their vicinity which influence the maintenance schedule. The dose rates are calculated at a point external to the diode casing. The ion diode material considered is stainless steel SS304LN and the penetration opening through the first wall to the diode is considered as 10 cm in radius. A schematic of a TDF diode is shown in Fig. 2.2.

Table 1.2. Publications

Reviewed Papers

1. D.L. Henderson, M.E. Sawan, and G.A. Moses, "Radiological Dose Calculations for the Diode Region of the Light Ion Fusion Target Development Facility," Fusion Tech. 0, 0 (1988).

Conference Proceedings

1. O. Yasar, M. Sawan, D. Henderson, and G. Moses, "Neutron Activation of the Light Ion Fusion Target Development Facility," Proceedings of the 12th Symposium on Fusion Engineering, Monterey, CA, Oct. 1987.
2. R. Peterson, R. Engelstad, D. Henderson, E. Lovell, G. Moses, M. Sawan, and O. Yasar, "Target Chamber Designs for the Light Ion Fusion Target Development Facility," Proceedings of the 12th Symposium on Fusion Engineering, Monterey, CA, Oct. 1987.
3. R. Olson, D. Cook, D. Bruggink, R. Engelstad, D. Henderson, E. Lovell, G. Moses, R. Peterson, M. Sawan, O. Yasar, "Conceptual Design of a High Gain Target Development Facility," Proceedings of the 12th Symposium on Fusion Engineering, Monterey, CA, Oct. 1987.

Fusion Technology Institute Reports

1. D.L. Henderson, "DKR-ICF: A Radioactivity and Dose Rate Calculation Code Package (Volume 1)," FTI Report UWFDM-714, November 1986, Revised April 1987.
   D.L. Henderson, "DKR-ICF: A Radioactivity and Dose Rate Calculation Code Package - Volume 2: Sample Problems for the DKR, CONVERT, and DOSE Codes," November 1986, Revised April 1987.
2. R. Holzer, "UWEOSPAC: A Subroutine Package for Accessing MIXERG-Generated SESAME-Formatted Multigroup Opacity Tables," University of Wisconsin Fusion Technology Institute Report UWFDM-721, March 1987.
3. O. Yasar, M. Sawan, D. Henderson, and G. Moses, "Radiological Dose Calculations for the Chamber and Diode Region of the Light Ion Fusion Target Development Facility," University of Wisconsin Fusion Technology Institute Report UWFDM-734, July 1987.
4. R. Peterson, R. Engelstad, E. Lovell, G. Moses, "Target Chamber Designs for the Light Ion Fusion Target Development Facility," University of Wisconsin Fusion Technology Institute Report UWFDM-733, October 1987.
5. B. Badger, et al., "Light Ion Beam Fusion Target Development Facility Studies: Progress Report for the Period 1 November 1986 to 31 October 1987," University of Wisconsin Fusion Technology Institute Report UWFDM-752, January 1988.

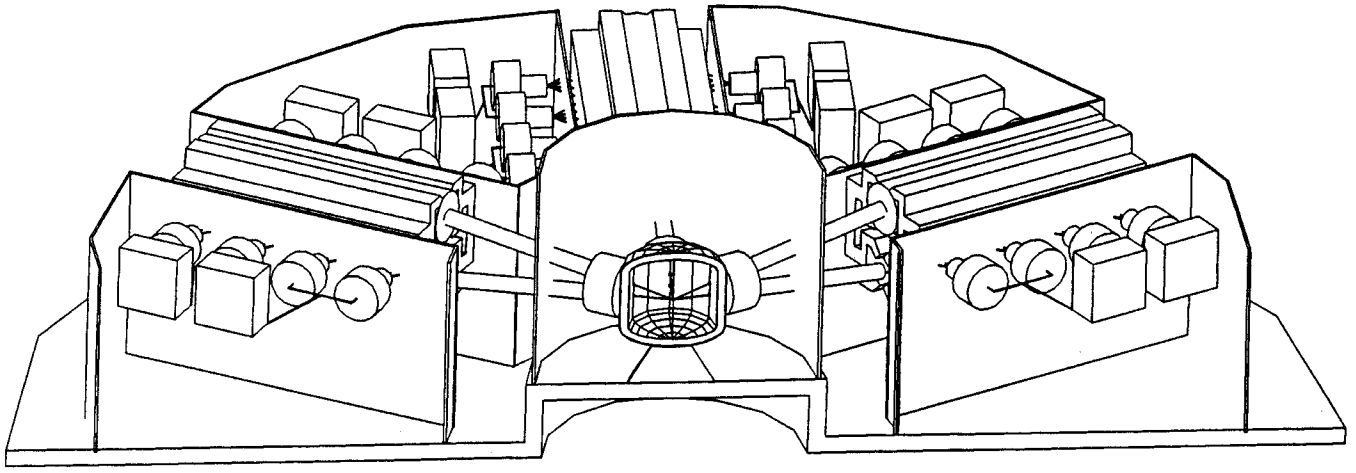

Fig. 2.1a. Preliminary design of the Light Ion Fusion Target Development Facility.

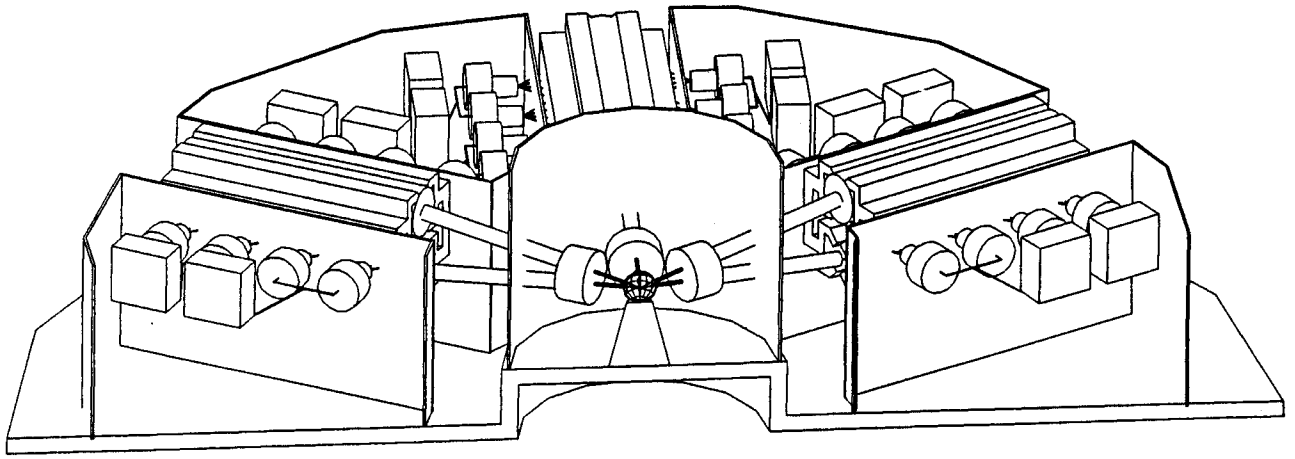

Fig. 2.1b. TDF chamber design with one meter radius chamber.

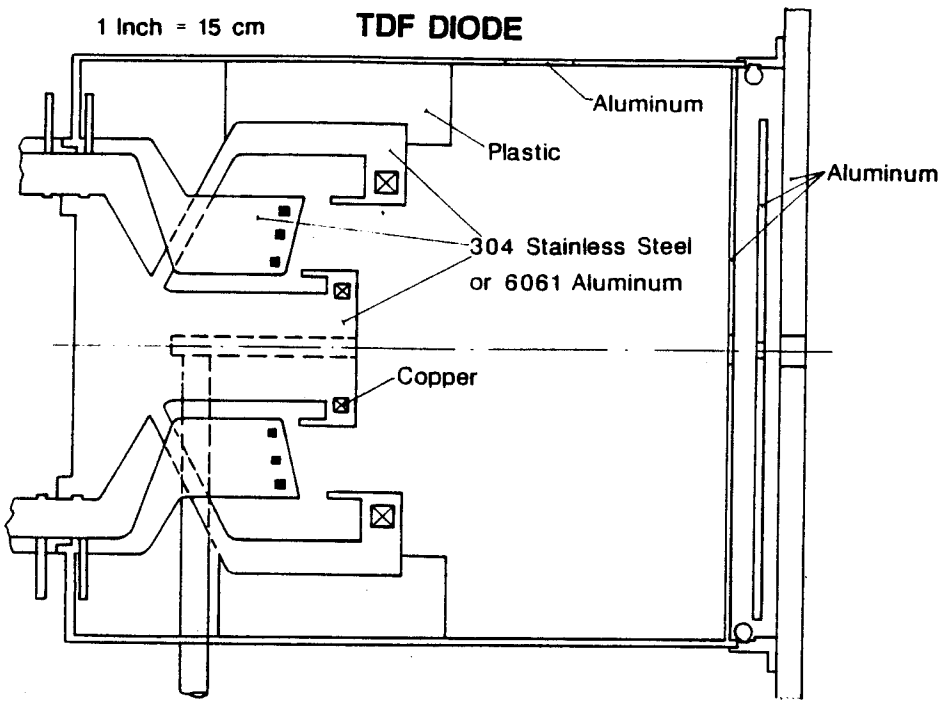

Fig. 2.2. Schematic of the high voltage ion diode used for the neutronic and dose rate calculations.

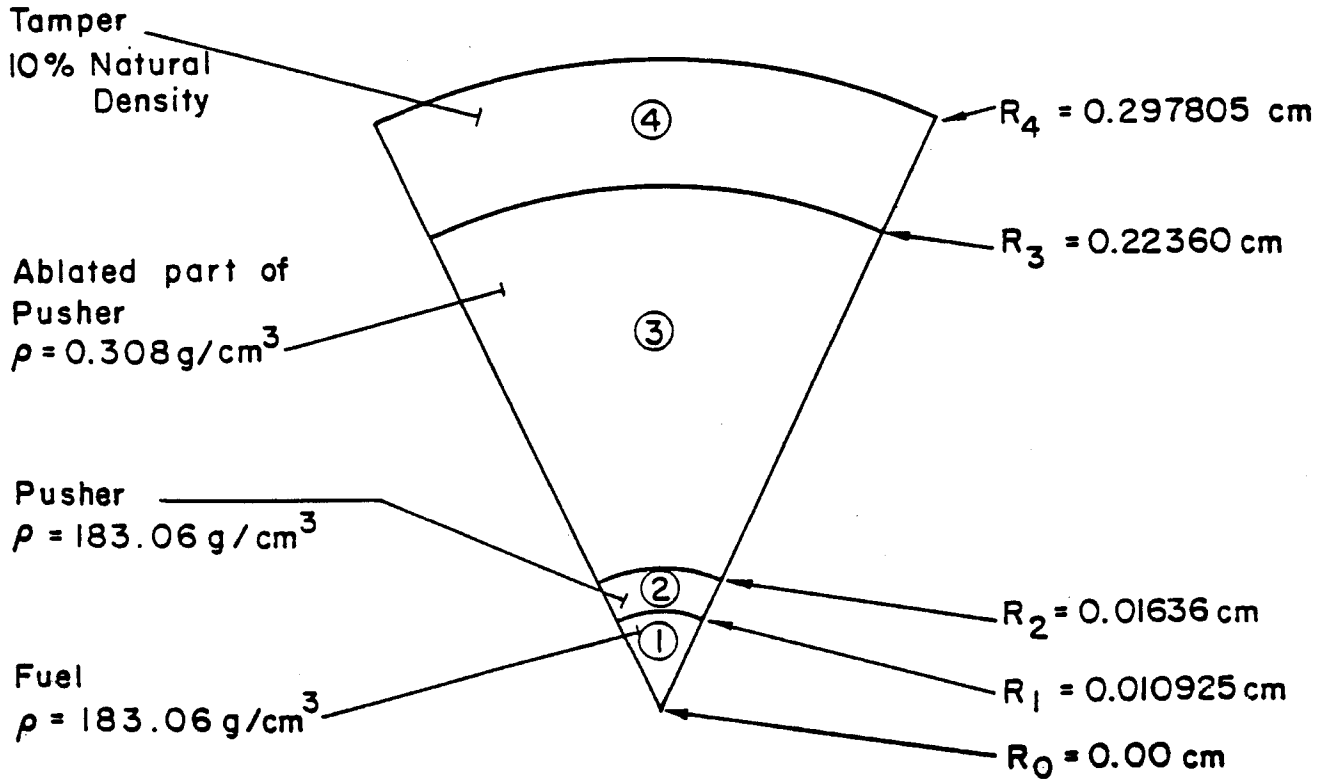

Fig. 2.3. The compressed target configuration used in the target neutronics calculations.

The dose rates in the diode region are calculated for both the three meter and the one meter chamber designs. The first wall material is taken as Al-6061-T6. Compared to the three meter case, the one meter chamber leaves room between the first wall and diode for shielding the diode region. Shielding materials considered are borated water, concrete and graphite. Among them, borated water shielding gives preferable results. The dose rate behind the first wall in the one meter chamber is significantly greater than the three meter chamber but the dose rate at the diode is less. This sets up a trade-off between early access to the chamber or to the diodes.

2.2 Neutron Transport Calculations

A consistent neutronics analysis must account for neutron target interactions which result in considerable spectrum softening of the fusion neutrons. The target DT load was assumed to be 1 mg and the fuel was assumed to be compressed to a density times radius product (ρR value) of 2 g/cm^2. The compressed target configuration used in the neutron transport calculations is shown in Fig. 2.3. A tamper density that is 10% of the natural density was used to account for the effect of heating by the impinging ion beams.

The spectrum of neutrons escaping from the target obtained from the target neutronics calculations is given in Fig. 2.4. For each D-T fusion, 1.046 neutrons leak from the target. A fuel burnup fraction of 30% was assumed, giving approximately 100 MJ of fusion energy released from the 1 mg fuel target used in the calculations. Since the TDF target is required to produce a yield of 200 MJ, a D-T mass of 2 mg will be needed. For the same ignition ρR value, intrinsic quantities such as neutron spectrum are assumed to not change while absolute quantities such as neutron yield are scaled by a factor of two. A 200 MJ target D-T yield corresponds to 7.09×10^{19} D-T fusions per shot and 7.42×10^{19} neutrons emanating from the target per shot. The neutron spectrum obtained from the target neutronics calculation was used to represent the source for the chamber neutronics.

The neutron flux in the diode is computed in two steps. First the cylindrically shaped target chamber is approximated by spherical geometry for a one-dimensional calculation. The TDF target chamber models used in the one-dimensional calculations are given in Fig. 2.5 for the three meter and one meter chamber designs. The first wall thickness is increased by 0.5 cm in the calculation model to account for the chamber structural support. The boral layers have boron enriched to 90% ^{10}B. The source is considered to be an isotropic point source at the center of the cavity. The neutron spectrum obtained from the target neutronics calculation was used to represent the source for the chamber calculation. The one-dimensional discrete ordinates code

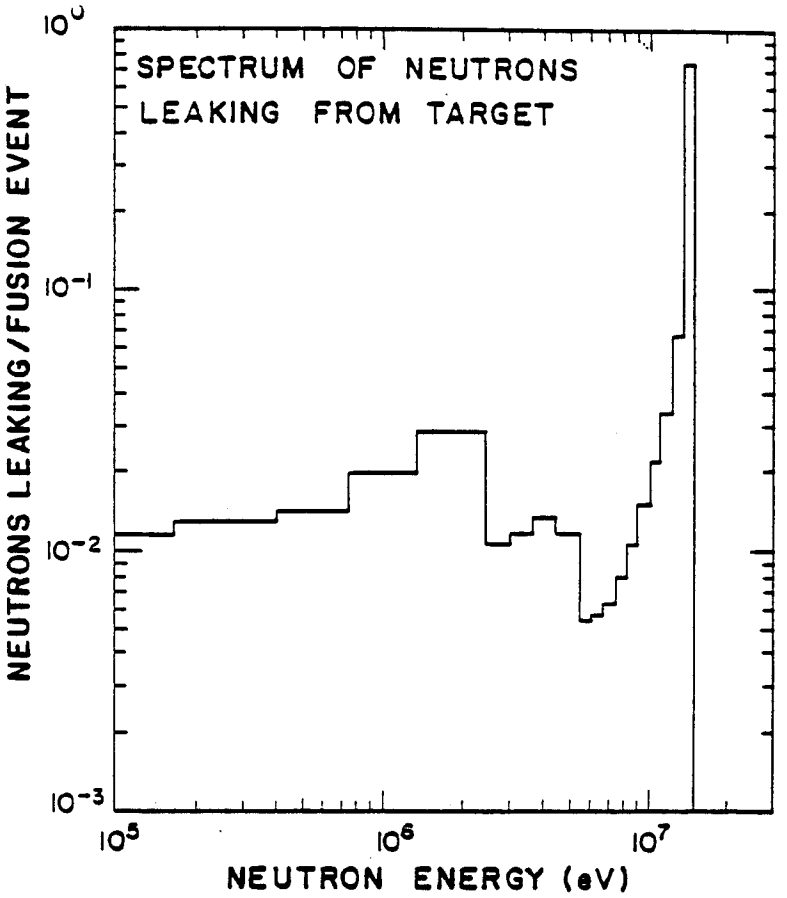

Fig. 2.4. Spectrum of neutrons emerging from the target.

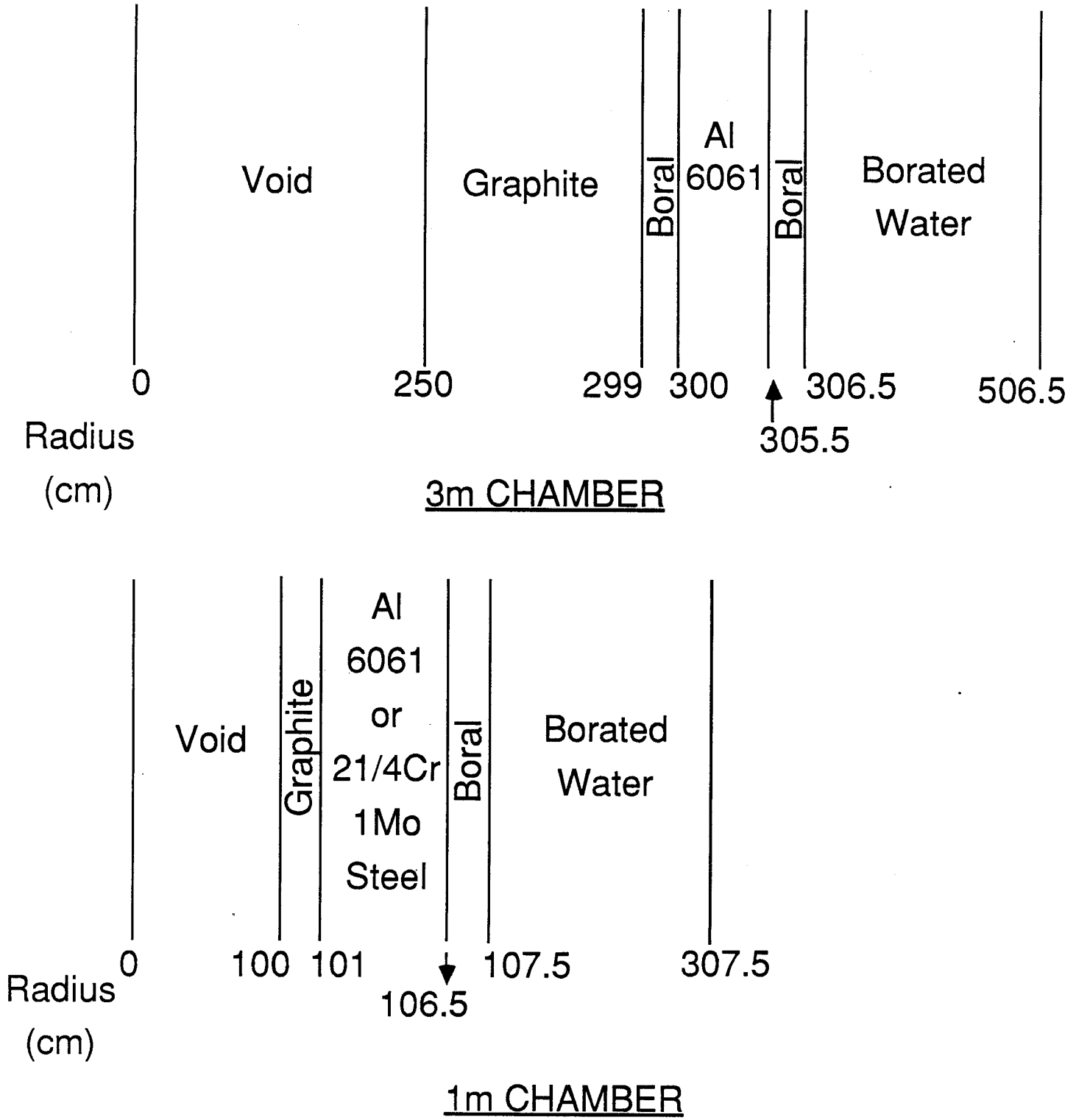

Fig. 2.5. One-dimensional schematic of the Target Development Facility one meter chamber design used for the neutronic and activation calculations.

ONEDANT[2] was used together with the LANL MATXS5[3] cross section data library processed from the ENDF/B-V evaluated file. The standard LANL 30 neutron-12 gamma group structure was used. The calculations were performed using the P_3-S_{16} approximation. The neutron flux obtained from the one-dimensional calculations was used to determine the wall activation and dose at the outer surface of the chamber wall.

The one-dimensional cavity calculation discussed above is used to obtain the energy and angular distribution of neutrons incident on the inner surface of the chamber. These are used to represent a surface source in the second step of the calculation where the detailed geometrical configuration of the diode is modeled. Since the beam ports occupy less than 2% of the inner surface area, the one-dimensional calculation in which the penetrations are not modeled gives a fairly accurate estimate of the nuclear radiation incident on the inner surface of the chamber and the beam penetration opening. In addition, since the diodes are located in the facility midplane, using spherical geometry in the one-dimensional calculation yields reasonably accurate results for nuclear radiation incident on the area around the beam ports.

The energy spectra of neutrons incident on the inner surface of the graphite are shown in Fig. 2.6 for the different chamber designs considered. The results represent the integral over all directions going into the graphite and are normalized to one D-T fusion and are given per energy group of the 30 neutron-12 gamma standard LANL group structure. Included also for comparison is the spectrum of neutrons emerging from the target. For each D-T fusion in the target, 1.046 neutrons emanate from the target and impinge directly on the inner surface of the chamber. Neutron scattering collisions in the surrounding materials results in reflecting some of these neutrons back into the cavity. These reflected neutrons will end up impinging on the graphite with a fraction of them reflected again into the cavity.

The total number of neutrons incident on the inner surface of the chamber for each D-T fusion is 6.929 for the three meter aluminum chamber. It is interesting to note that this is slightly higher than that obtained for the previous preliminary design when the inner surface of the graphite was at a smaller radius with scattered neutrons having a smaller probability of reentering the cavity. The corresponding numbers for the one meter chamber with Al and steel walls are 1.553 and 2.065, respectively. The significantly smaller amount of neutrons reentering the cavity in the one meter chamber case is related to the smaller cavity radius and less reflection by the thin graphite liner. Only 15% of the total impinging neutrons came directly from the target in the three meter chamber case resulting in a spectrum that is much softer than that emerging from the target. Harder neutron spectra are obtained in the one meter chamber case with the

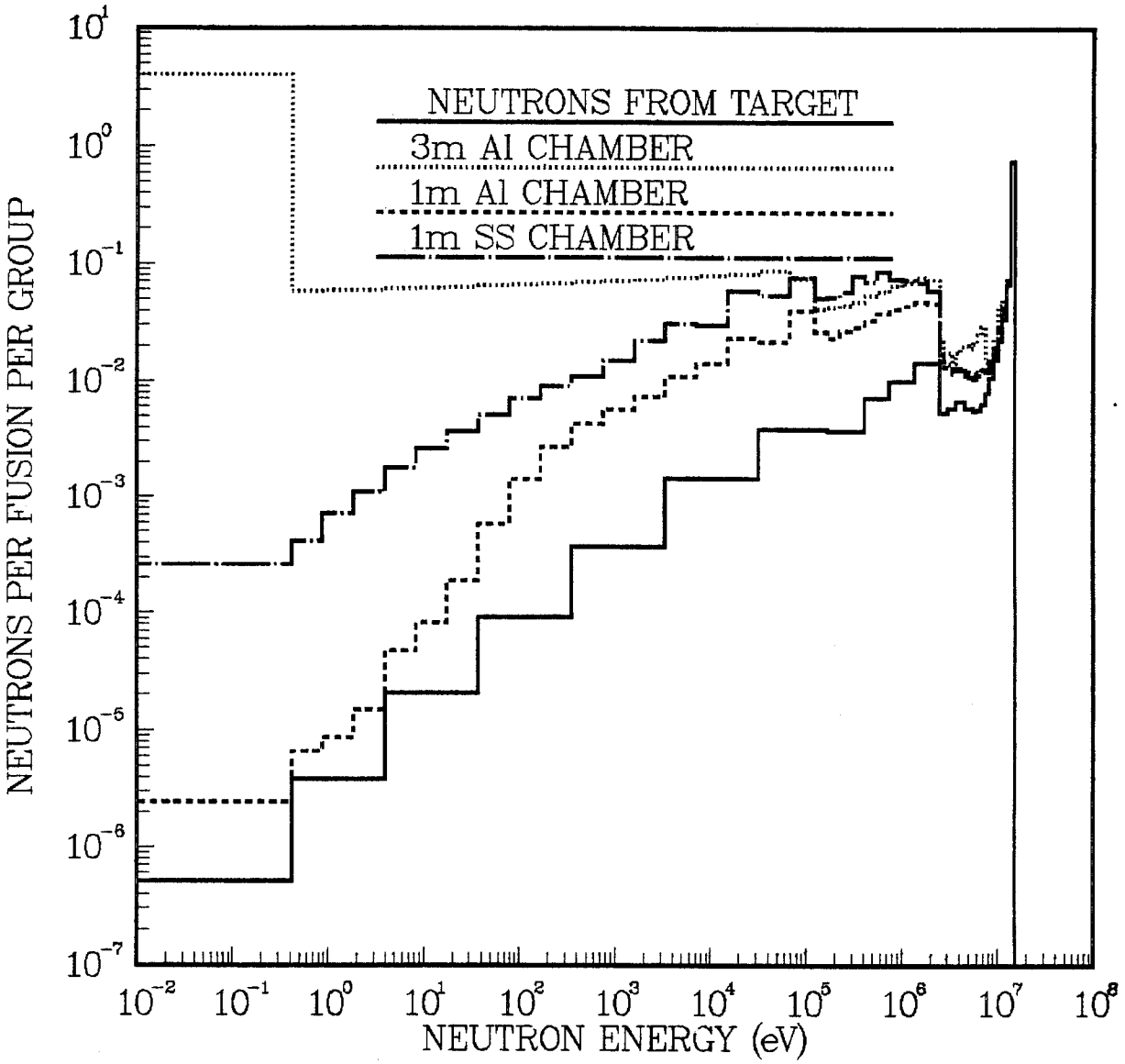

Fig. 2.6. Energy spectra of neutrons incident on front surface of graphite in TDF.

uncollided neutrons representing 67% and 50% of the total number of neutrons for the Al and steel walls, respectively. It should be pointed out that the angular distribution of incident neutrons varies from one energy group to the other. Peaking in the normal direction is more pronounced for high energy groups where the direct contribution from the target is large. The energy spectra of neutrons incident on the liner in the discrete ordinates directions are stored to serve as surface source distributions in the two-dimensional calculation that properly models the detailed diode geometry. A relatively large S_N order of 16 is used here for proper representation of the angular distribution of neutrons incident on the inner surface of the chamber.

Two-dimensional neutronics calculations have been performed to determine the flux distribution in the diode. The diode geometry was modeled in two-dimensional r-z geometry. Calculations have been performed for both the three meter and one meter chamber designs. The cathode and anode are made of stainless steel 304LN and the penetration radius is 10 cm. Three calculations have been performed for the one meter chamber case with three different shielding materials, namely borated water, concrete, and graphite being used in the space between the first wall and the diode. Hence, a total of four two-dimensional neutronics calculations has been performed. Figs. 2.7 and 2.8 give the r-z geometrical models used in the calculations for the three meter and one meter chamber cases, respectively.

The two-dimensional discrete ordinates code TWODANT[4] was used in the calculations with the same 30 neutron-12 gamma multigroup cross section data based on the ENDF/B-V evaluation which was used in the one-dimensional calculation. A spatially uniform surface source was used at the bottom boundary represented by the energy dependent angular flux at the inner surface of the chamber as obtained from the appropriate one-dimensional calculation. The source is given in the eight discrete ordinates directions going into the graphite region. The source is assumed to be uniform in the azimuthal direction. A vacuum boundary condition is used at the bottom boundary since the contribution from neutrons reentering the cavity from the surrounding materials is already taken into account in the surface source. A vacuum boundary is also used at the top. A right reflecting boundary is used in the calculational model to account for the interaction between adjacent penetrations. This boundary should be located at half the distance between the adjacent penetrations. In the actual geometry this distance increases as one moves from the inner surface of the chamber to the diode. However, the two-dimensional r-z geometry allows only for a cylindrical reflecting boundary as shown in Figs. 2.7 and 2.8. Furthermore, while the spacing is smaller at the inner surface of the one meter chamber than that in the three meter chamber, it is

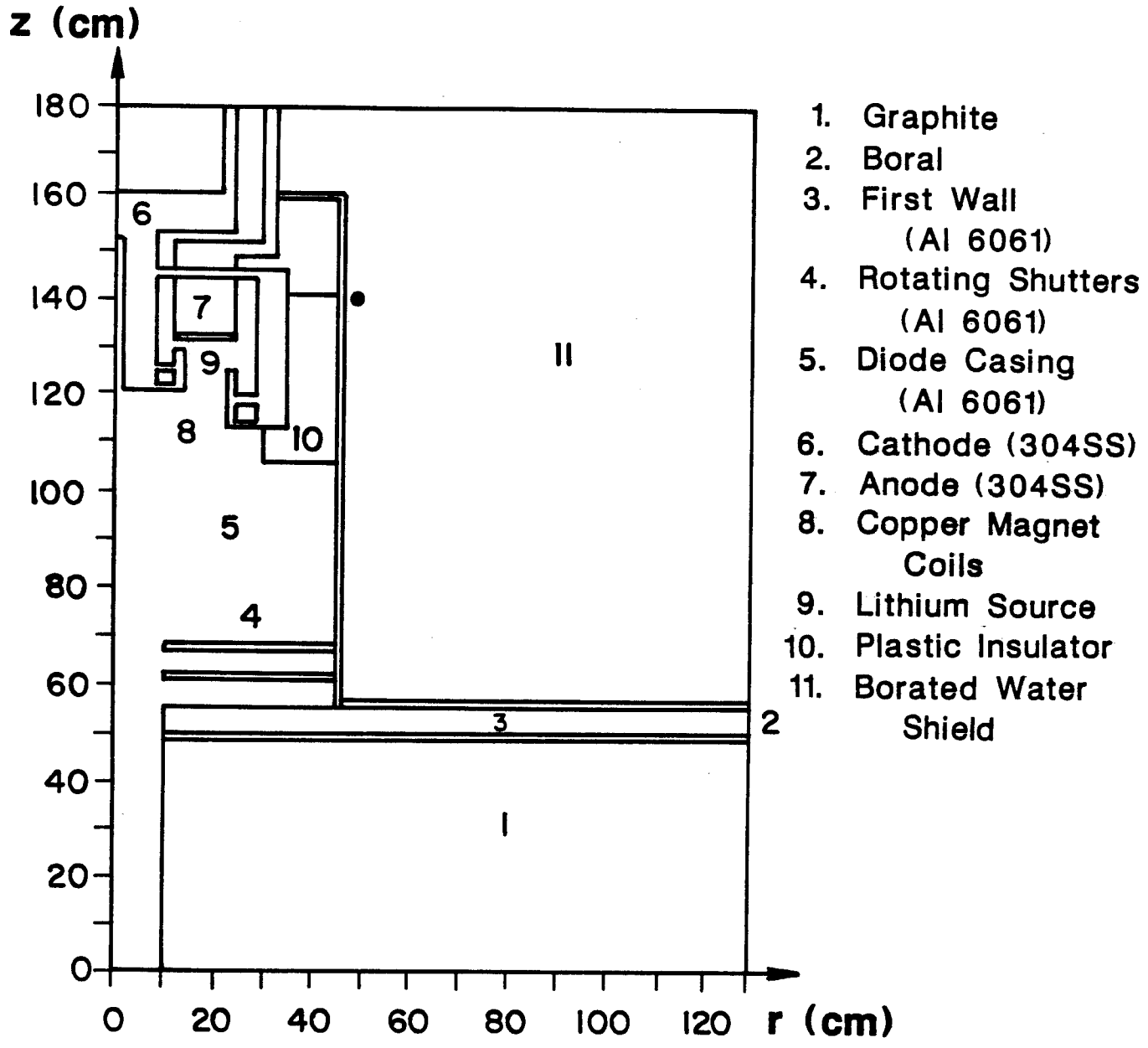

Fig. 2.7. The r-z geometrical model used in the two-dimensional neutronics and activation calculations for the three meter chamber design.

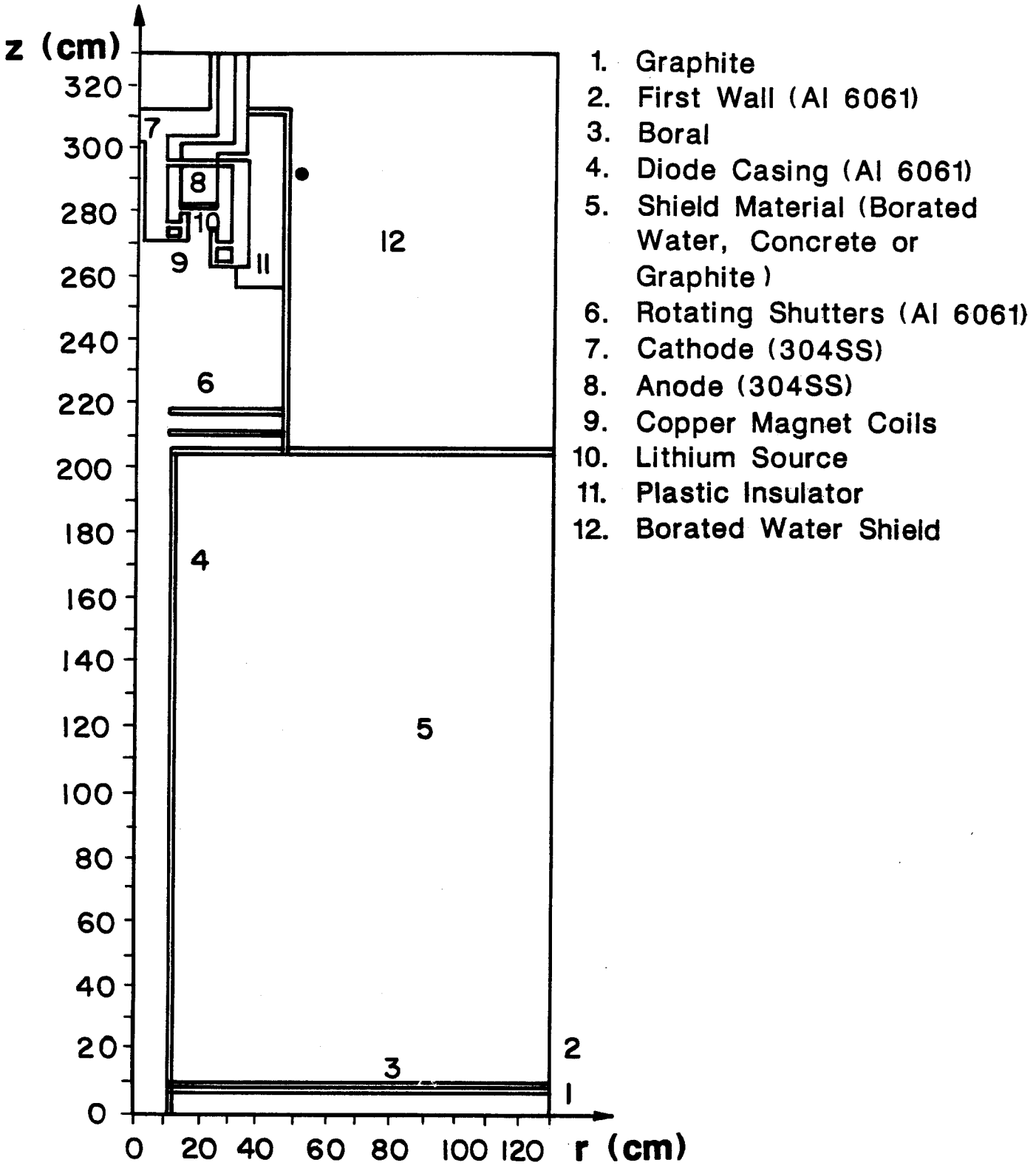

Fig. 2.8. The r-z geometrical model used in the two-dimensional neutronics and activation calculations for the one meter chamber design.

identical at the diodes which are located at the same distance from the target in both cases. In the three meter chamber case the reflecting boundary is taken at a radius of 125 cm which is the distance between the penetration centerline and the plane of symmetry between adjacent penetrations at the inner surface of the graphite region. This is expected to give conservative estimates for the flux in the diode due to the larger shielding space between adjacent diodes. In the one meter chamber case the distance between the penetration centerline and the plane of symmetry between adjacent penetrations is 50 cm at the inner surface of the graphite liner and increases rapidly to values larger than 125 cm in the diode region. The sensitivity of the calculated flux to the location of the reflecting boundary was determined by performing calculations for reflecting boundaries at radii of 50 and 125 cm. The flux in the 10 cm radius beam duct was found to not be sensitive to the location of the reflecting boundary due to the large shielding space between adjacent penetrations even for the 50 cm radius reflecting boundary. On the other hand, the 50 cm radius reflecting boundary results in overestimating the flux in the diode by up to ~60% since only 8 cm of shielding space is provided between adjacent diodes in this case. Since the spacing between diode centerlines is larger than 125 cm in the actual design, a reflecting boundary radius of 125 cm is also used for the one meter chamber calculational model.

It should be noted that the use of a cylindrical reflecting boundary is equivalent to surrounding the modeled diode by diode penetrations at all azimuthal locations. This tends to overestimate the flux and dose in the diode area. Furthermore, using an r-z model with a planar disc source at the bottom boundary does not take into account the geometrical attenuation of the flux which can be significant particularly for the component coming directly from the target at the center of the cavity. The $1/R^2$ geometrical attenuation implies an attenuation factor of ~ 12 for the flux as one goes from the front of the graphite liner to the front of the diode for the one meter chamber. It is clear, therefore, that the geometrical approximations introduced by the two-dimensional model tend to give conservative estimates for the flux and dose in the diode region. The only way to avoid these geometrical modeling deficiencies is to use the Monte Carlo method where the detailed three-dimensional geometry can be modeled. However, the Monte Carlo method is statistical in nature and is not capable of generating accurate estimates for differential quantities such as the neutron energy spectra in optically thin zones which are required for activation and dose calculations.

In addition to the forward neutron transport calculations, adjoint gamma transport calculations were performed for the four cases considered here. In the adjoint calculations, an adjoint source was used on the outer surface of the diode casing with the

energy spectrum given by the gamma flux-to-dose conversion factors. The location of the source is taken at the location where the dose after shutdown is calculated. This position outside the diode casing is at a radius of 47 cm and at a distance of 392 cm from the center of the cavity. These calculations were used to determine the adjoint dose field distribution that is coupled with the decay gamma source to yield the dose at this position for various times after shutdown.

2.3. Dose Rate Calculations

2.3.1 Libraries and Codes

The dose rate calculations were performed using the DKR-ICF[5] code package which consists of the radioactivity calculation code DKR, the data handling code CONVERT and the dose rate calculation code DOSE. The spatial models used for radioactivity and dose calculations are identical to the model used for the TWODANT neutronic calculations and are given in Figs. 2.5, 2.7, and 2.8. The large dot drawn in the figures designates the point at which the dose rate is calculated.

ACTLLIB, a decay and neutron transmutation data library based on the evaluated neutron activation cross section library ACTL[6], is used as the primary database for the activation calculations. The neutron transmutation data is given in a 46 group structure format. The decay and gamma source data is taken from the Table of Isotopes[7] with the gamma source data being in a 21 group structure format. Tables 2.1 to 2.3 give the composition of the materials used in the calculations. The radioactivity and dose calculations take 2-5 minutes of Cray-XMP/48 time per case. This is a great advantage for current and future two-dimensional radioactivity and dose calculations compared to previous studies[8] that have taken 9-10 hours of Cray-XMP/48 time. Code optimization in the reference to data libraries has resulted in this cost savings.

2.3.2 Dose Rate Results

The dose rate results are presented for various designs of chamber wall, chamber structure and shielding materials. Results are normalized to 200 MJ of target yield. The operation of the facility is assumed to be 12 shots per day for five days per week for four weeks, totaling one month of operation.

The dose rates behind the chamber wall due only to the chamber and borated water are given in Fig. 2.9. At short times after shutdown (up to one week) the dose rate behind the aluminum wall for the one meter case exceeds the stainless steel dose rates. Thereafter, it drops below it up to 10 years. The initial shape of both one meter curves up to approximately one day after shutdown shows the same behavior and is determined by the decay of short-lived isotopes $^{28}_{13}Al$, $^{27}_{12}Mg$ and $^{26}_{11}Na$ in aluminum and $^{28}_{13}Al$

Table 2.1. Chamber Wall Constituent Densities

2-1/4 Cr-1 Mo Steel		Aluminum-6061-T6	
Element	Density [atoms/b-cm]	Element	Density [atoms/b-cm]
C	4.3135×10^{-4}	Mg	6.6889×10^{-4}
Si	6.7080×10^{-4}	Al	5.8192×10^{-2}
P	3.0413×10^{-5}	Si	3.4741×10^{-4}
S	2.9379×10^{-5}	Ti	5.0925×10^{-5}
Ti	2.9499×10^{-5}	Cr	9.3827×10^{-5}
V	2.7737×10^{-5}	Mn	4.4401×10^{-5}
Cr	1.9928×10^{-3}	Fe	2.0383×10^{-4}
Mn	4.2866×10^{-4}	Cu	7.6781×10^{-5}
Fe	8.0452×10^{-2}	Zn	6.2193×10^{-5}
Cu	1.4825×10^{-4}		
Mo	4.9093×10^{-4}		

Table 2.2. Composition of Materials Comprising the Diode, First Wall, Boral, and Graphite Moderator Regions

Element (wt.%)	Oxygen Free-High Conductivity Copper ρ = 8.96 g/cm^3	SS304LN (Diode Material) ρ = 8.03 g/cm^3	Al-6061-T6 (Chamber Wall) ρ = 2.7 g/cm^3
H	0.0002	---	---
B	---	---	---
C	---	0.022	---
N	---	0.149	---
O	0.0003	---	---
Mg	---	---	1.0
Al	---	---	96.55
Si	---	0.62	0.60
P	0.0003	0.019	---
S	0.002	0.005	---
Ti	---	--	0.15
V	---	---	---
Cr	---	18.31	0.30
Mn	0.00004	1.33	0.15
Fe	0.001	69.73	0.70
Co	---	0.19	---
Ni	0.0013	9.30	---
Cu	99.9905	0.16	0.30
Zn	0.001	---	0.25
As	0.0003	---	---
Mo	---	0.17	---
Ag	0.0025	---	---
Cd	0.0001	---	---
Sn	0.0003	---	---
Sb	0.0008	---	---
Te	0.0002	---	---
Pb	0.0008	---	---

Table 2.2. (continued)

Element (wt.%)	Graphite H-451 ρ = 1.74 g/cm^3	Boral (Enriched with B^{10}) ρ = 2.53 g/cm^3	Plastic ρ = 0.95 g/cm^3	Lithium ρ = 0.534 g/cm^3
H	---	---	8.16	---
Li	---	---	---	100
B	---	16.8	---	---
C	100	4.9	48.64	---
O	---	---	43.20	---
Al	---	78.2	---	---

Table 2.3. Composition of Shield Materials: Borated Water, Concrete and Graphite

Element (wt.%)	Borated Water ρ = 2.53 g/cm^3	Concrete ρ = 2.32 g/cm^3	Graphite ρ = 1.74 g/cm^3
	Density [atoms/b-cm]		
H	6.85 e-02	1.24 e-02	---
Al	---	9.28 e-04	---
O	3.50 e-02	3.91 e-02	---
Fe	---	6.95 e-03	---
Mn	---	3.13 e-05	---
Ti	---	1.27 e-05	---
B-10	4.42 e-04	---	---
B-11	4.91 e-05	---	---
K	---	2.33 e-05	---
Ca	---	6.96 e-03	---
Na	---	2.22 e-04	---
Mg	---	7.40 e-04	---
N	---	8.70 e-06	---
S	---	6.44 e-05	---
C	---	5.68 e-03	8.73 e-02

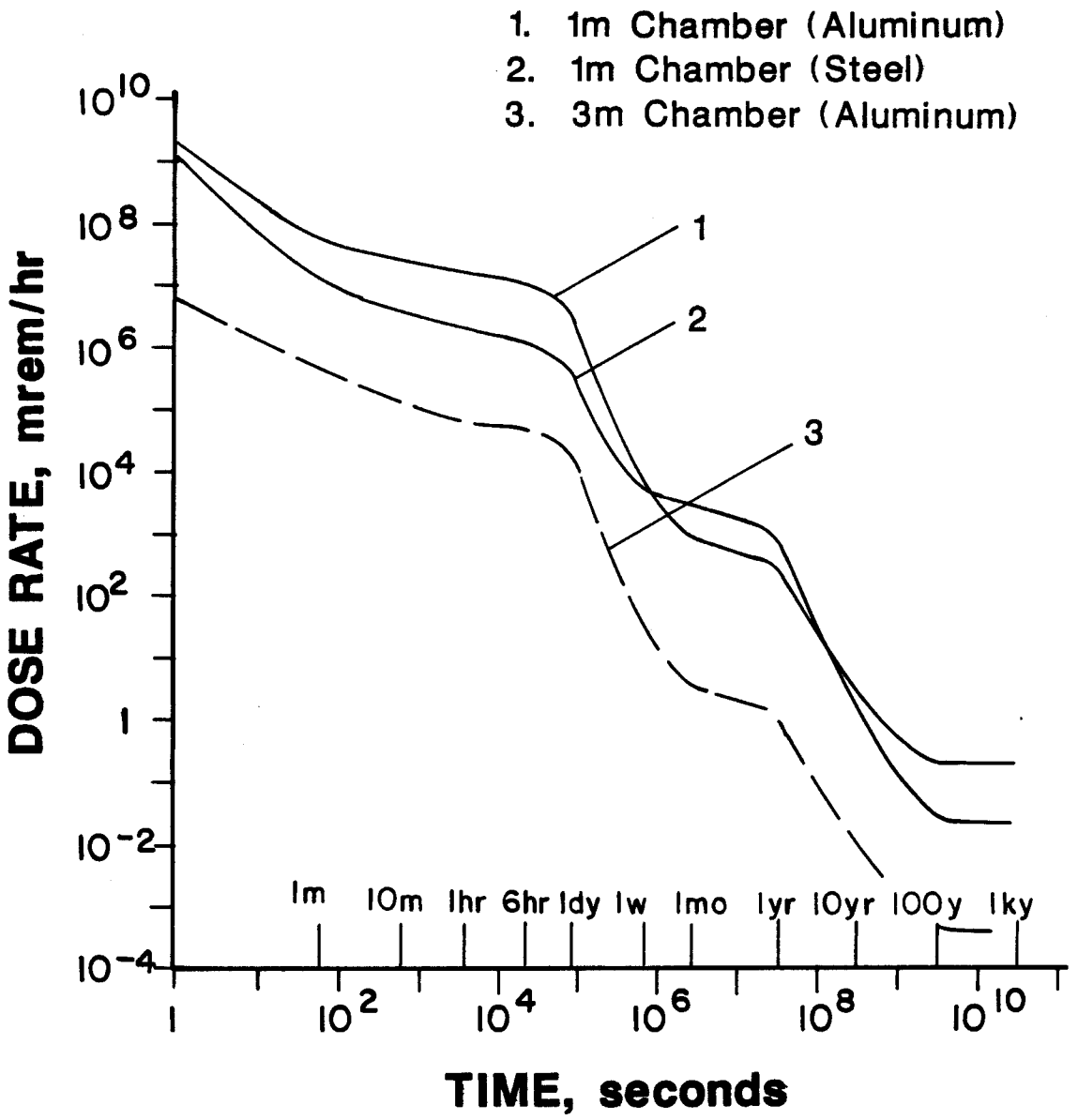

Fig. 2.9. Dose rates behind the first wall.

and $^{56}_{25}Mn$ in stainless steel. The large drop in the aluminum dose rate after one day following the shutdown is the result of the decay of $^{24}_{11}Na$ which has a half-life of 15 hours. The three meter chamber with an aluminum first wall has a similar curve to the one meter case, except the level for the three meter case is more than two orders of magnitude lower due to the reduced high energy neutron flux level. This flux has been reduced by the inclusion of 50 cm of graphite within the target chamber.

Figure 2.10 shows the dose rate results at a position near the diode, as shown in Figs. 2.7 and 2.8, for different shielding materials. The dashed line is for the three meter design and the other three curves are for the one meter design with various shield materials. The diode material considered is SS304LN stainless steel and the chamber wall material is Al-6061-T6. Among the different shield materials, borated water (with boron enriched to 90% $^{10}_{5}B$) is the best for almost all times after shutdown. The lower the level of neutron flux in the diode region, the fewer neutron transmutations that there will be and thus the lower the decay gamma dose level in the system. The dose rate at one week after shutdown is 3.7 mrem/hr for the borated water shielding case. The corresponding values for the concrete and graphite shielding cases are 3.83 and 5.8 mrem/hr, respectively.

A comparison is made between the dose rates of the three meter and one meter designs and is shown in Fig. 2.11. When comparing the dose rates behind the aluminum first wall, it is quite clear that the dose for the one meter chamber wall is much higher, since the one meter chamber wall is much closer to the target than the three meter chamber and there is no neutron moderator inside. Due to the higher neutron flux, the number of neutron transmutations and thus the number of gamma producer elements is higher for the one meter case. The dose rate at one week after shutdown is 8.4 rem/hr for the one meter chamber wall and is 34.5 mrem/hr for the three meter chamber wall. However, since there is a large shielding space between the one meter chamber wall and the diode, the dose level at the diode region is lower for the one meter chamber than the dose level at the diode region for the three meter chamber. With any shielding material in the one meter case, the dose rate is in the range of 3-6 mrem/hr at one week after shutdown, whereas it is 25 mrem/hr for the three meter case.

The dose contribution from each component of the system is also of interest. Figures 2.12 and 2.13 show the dose rate contribution of each component to the dose rate at the point in the diode region. These components are the aluminum first wall, boral, liner, plastic insulator, copper coils, aluminum casing, shield material and the diode material (SS304LN). As observed from the previous studies,[8] the main contribution several days after shutdown comes from just the diode material SS304LN. This is due to

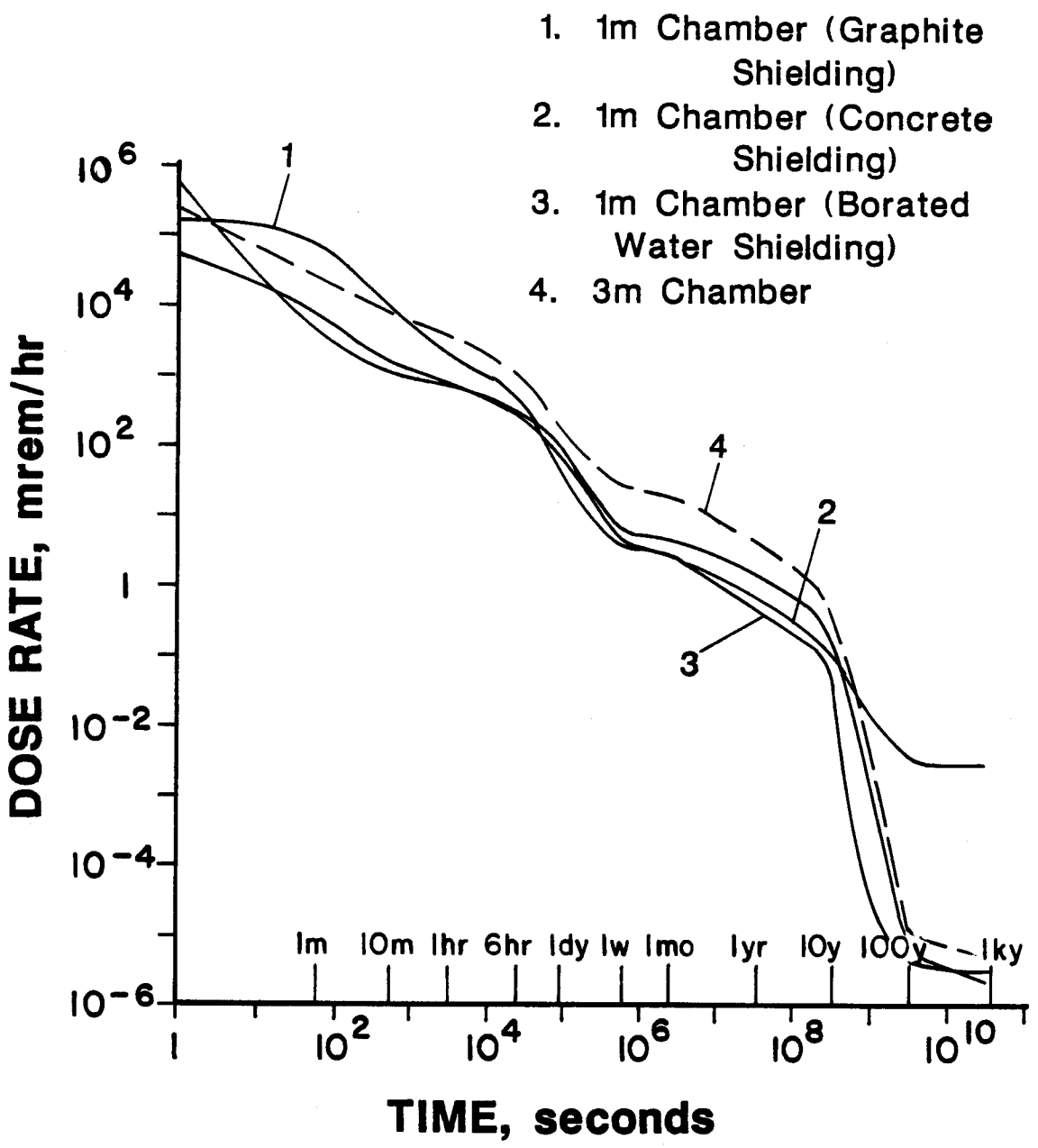

Fig. 2.10. Dose rates at the diode region for both one meter and three meter designs with Al first wall.

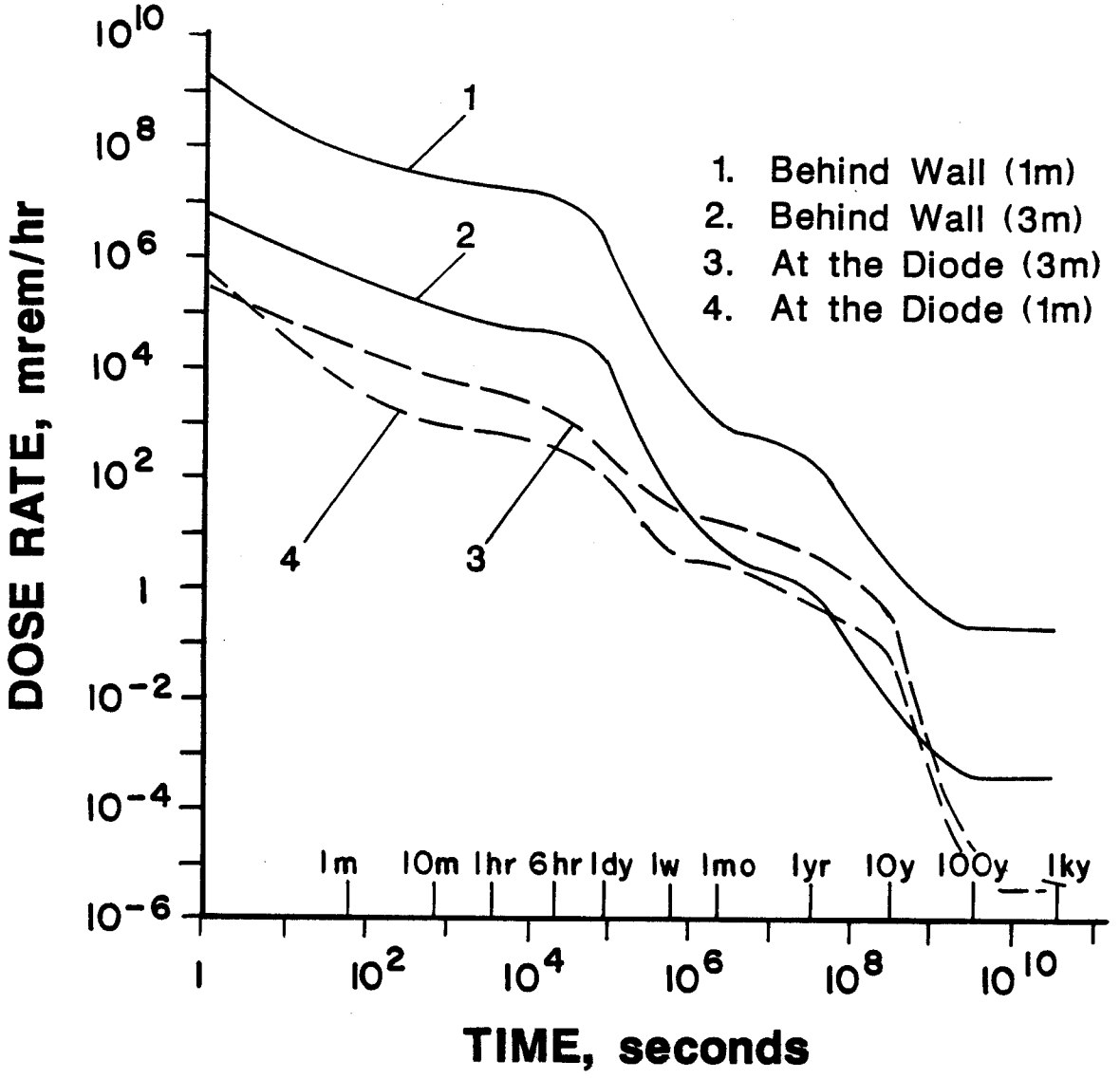

Fig. 2.11. Chamber wall and diode region dose rate comparison for one meter and three meter chamber designs.

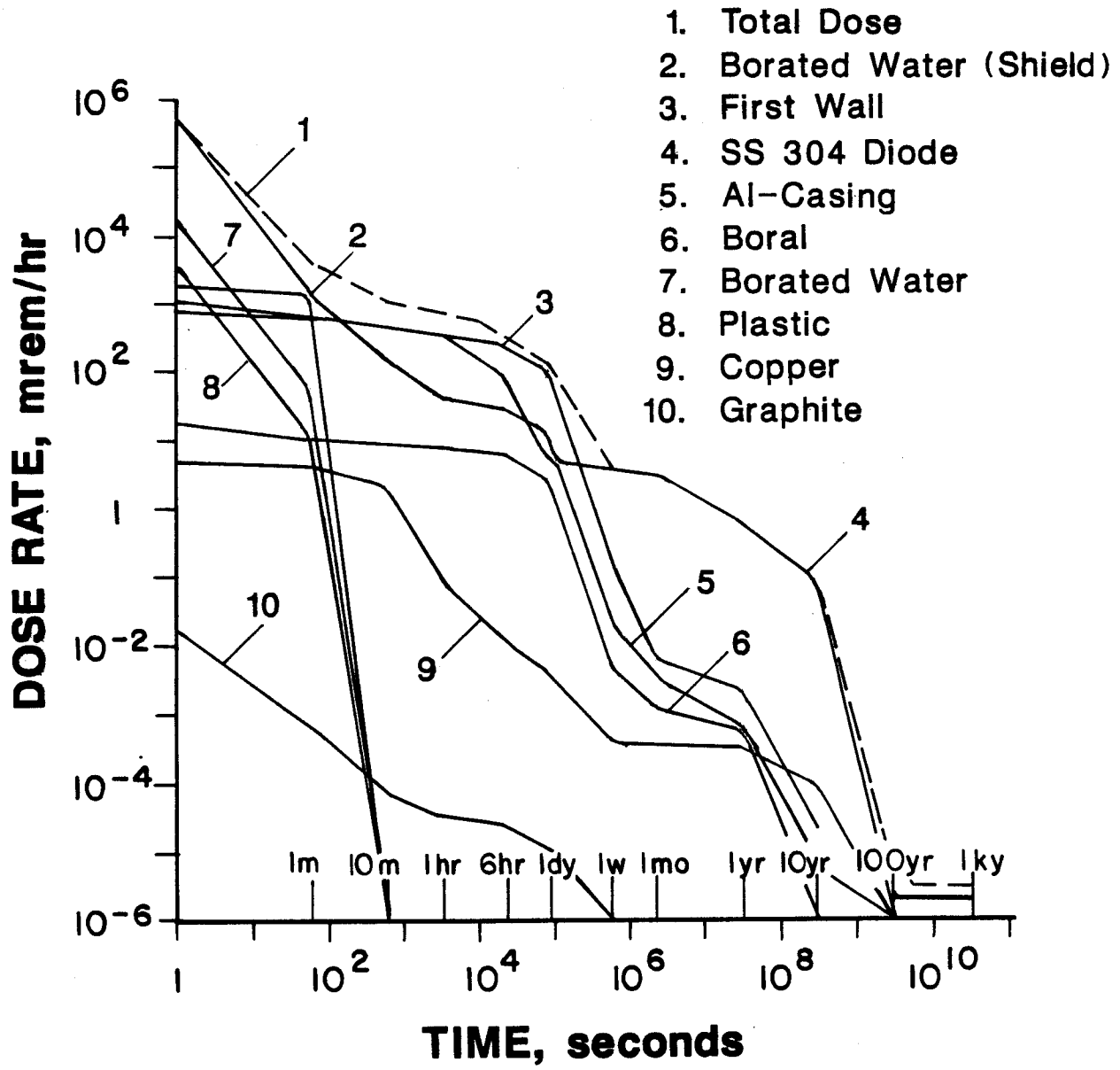

Fig. 2.12. Contributions from each component to the dose at the diode region for the one meter chamber design.

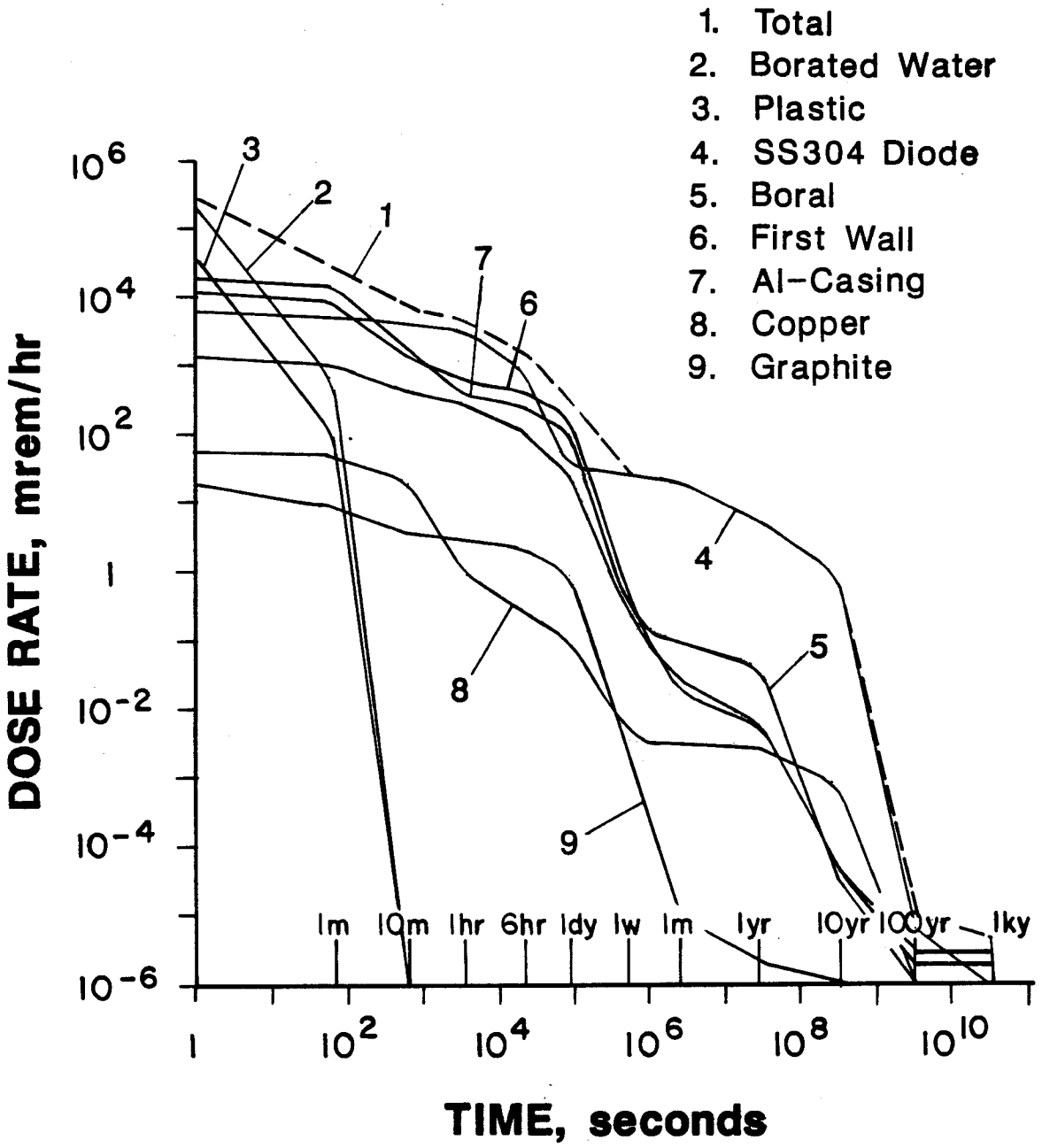

Fig. 2.13. Contributions from each component to the dose at the diode region for the three meter chamber design.

long-lived elements $^{51}_{24}Cr$, $^{54}_{25}Mn$, $^{57}_{27}Co$, $^{58}_{27}Co$. On the other hand, the other components such as plastic and borated water, that produce the short-lived element $^{16}_{7}N$ whose half-life is 7.1 seconds, contribute nothing after 4-5 minutes following the shutdown. The components containing a high percent of aluminum (boral, aluminum first wall and casing) follow the same behavior. The drop after one day is due to the decay of $^{24}_{11}Na$.

It is therefore clear that the dose at the diode is dominated by the borated water and plastic activation at short times following shutdown and by the activation of the first wall, boral and diode casing at intermediate times. The long term dose is mainly due to activation of the steel in the diode. This explains the results of Fig. 2.11 which show the dose at the diode to be higher for the one meter chamber case than the three meter chamber case at short times following shutdown. This is due to the fact that more borated water is used in the one meter chamber case. At intermediate times after shutdown, the dose rate for the one meter chamber case is about a factor of three lower than that for the three meter chamber case, because of the additional shielding between the aluminum first wall and the diode that provides some attenuation for the decay gammas produced in the first wall and the neutrons that activate the aluminum diode casing. At long times following shutdown, the dose is dominated by the activity produced in the steel diode which is not very much affected by the additional shield used in the one meter chamber case since a large part of the diode is in direct line of sight of source neutrons. Hence, using the one meter chamber results only is a modest drop in the dose rate at long times after shutdown.

2.4. Summary

The neutronics, radioactivity and dose rate calculations for the Light Ion Fusion Target Development Facility have been performed. The biological dose rates were computed behind the first wall and at a point external to the diode casing following an operational period of one month. Two different chamber designs, one meter and three meter, were examined. The primary first wall and diode materials considered were Al-6061-T6 and SS304LN, respectively. The penetration through the wall to the diode has been taken as 10 cm in radius. Different shield materials were considered in the space between the one meter chamber and the diodes. These included borated water, graphite and concrete. Using borated water resulted in the lowest dose rate in the diode region one week after shutdown. At this time the dose rate at the outer surface of the diode casing is 3.7 mrem/hr which is lower than the 24.5 mrem/hr dose rate obtained for the three meter chamber design. On the other hand, the dose rate behind the Al first wall in the one meter chamber design is 8.4 rem/hr one week after shutdown which is much larger

than the 34.5 mrem/hr value obtained in the three meter chamber design. All components of the facility contribute significantly to the dose level measured in the vicinity of the diode up to one week following shutdown but only the diode material (SS304LN) contributes significantly to the dose level after that time. The low dose rate in the diode region for the one meter chamber design implies that hands-on maintenance of the diode might be possible. However, remote handling of the stainless steel diode is necessary in the three meter chamber design. Once the diode has been remotely removed, manual access to the diode casing is possible at one week after shutdown.

References for Section 2

1. D.L. Henderson, G.A. Moses, R.R. Peterson, "One-Dimensional Activation and Radiological Dose Calculations for the Light Ion Fusion Target Development Facility," University of Wisconsin Fusion Technology Institute Report UWFDM-636 (1985).

2. R.D. O'Dell et al., "User's Manual for ONEDANT: A Code Package for One-Dimensional, Diffusion-Accelerated, Neutral-Particle Transport," LA-9184-M, Los Alamos National Laboratory (Feb. 1982).

3. R. MacFarlane, "Nuclear Data Libraries from Los Alamos for Fusion Neutronics Calculations," Trans. Am. Nucl. Soc. 46, 271 (1984).

4. R. Alcouffe et al., "User's Guide for TWODANT: A Code Package for Two-Dimensional, Diffusion-Accelerated, Neutral-Particle Transport," LA-10049-M, Los Alamos National Laboratory (March 1984).

5. D.L. Henderson and O. Yasar, "DKR-ICF: A Radioactivity and Dose Rate Calculation Code Package," University of Wisconsin Fusion Technology Institute Report UWFDM-714 (1986).

6. M.A. Gordinier and R.J. Howerton, "ACTL: Evaluated Neutron Activation Cross Section Library Evaluation Techniques and Reaction Index," UCRL-50400, Vol. 18 (1978).

7. C.M. Lederer et al., Table of Isotopes, Sixth and Seventh Editions, Wiley (1967 and 1978).

8. D.L. Henderson, M.E. Sawan, G.A. Moses, "Radiological Dose Calculations for the Diode Region of the Light Ion Fusion Target Development Facility," University of Wisconsin Fusion Technology Institute Report UWFDM-707 (1986).

3. FINITE ELEMENT STRUCTURAL ANALYSIS

3.1. Introduction

Stresses and deflections have been determined for the TDF reaction chamber using finite element methods. The effort serves to identify the degree of refinement necessary for accurate results and the utility of the method for analyzing more complicated loadings or geometries, such as the beam ports in the chamber wall.

3.2. Axisymmetric Chamber

For the vessel initially considered, both the diameter and length are six meters. Boundary conditions prescribed at each end require no radial or tangential displacement components. Surface slope changes are also zero at both ends. Relative axial displacements are allowed so as to model the case of a shell supported at the bottom but free to extend at the top. (Other cases which did not represent the physical chamber were also analyzed to verify a number of particular aspects of the code. These problems included simply supported boundary conditions as well as ends with all six degrees of freedom constrained.) The characteristics of the relevant basic cases are listed in Table 3.1. The objective with these was to establish the minimum number of elements necessary for good accuracy. In general, results from the first two cases were not sufficiently accurate. For case three, stresses were acceptable except near the ends. In the physical problem, high stress gradients occur in these regions. Thus local refinements were made, corresponding to case 4 and shown in Fig. 3.1. Additional improvements could be achieved by more circumferential divisions in the end elements to make their aspect ratio closer to unity. However, the extra time and expense did not justify this.

3.3. Comparison of Results for the Reaction Chamber

For these computations the length, radius and thickness are six meters, three meters and three cm, respectively, for an aluminum chamber with an overpressure of one MPa. Classic theory is applied to obtain a closed-form solution using these parameters. Longitudinal normal stress profiles are shown in Fig. 3.2 for the lower half of the chamber. Excellent agreement between the finite element results and the exact solution is apparent even through the severe flexural gradient at the end. Similarly, finite element results for circumferential normal stress are plotted in Fig. 3.3. Over the central two thirds of the vessel, uniform membrane stress of 100 MPa is the principal component (i.e., the pressure amplified by the radius/thickness ratio). Near the ends, tensile and compressive flexural stress increase rapidly. The total stress shown for the inner and outer surfaces consists of these and the tensile membrane stress.

Table 3.1. Characteristics of Basic Finite Element Cases

Basic Case	1	2	3	4
Axial Divisions	6	12	12	24
Circumferential Divisions	24	36	45	45
Element Total	144	432	540	1080
Element Size (cm)	100x79	50x52	50x42	50x42/12.5x42

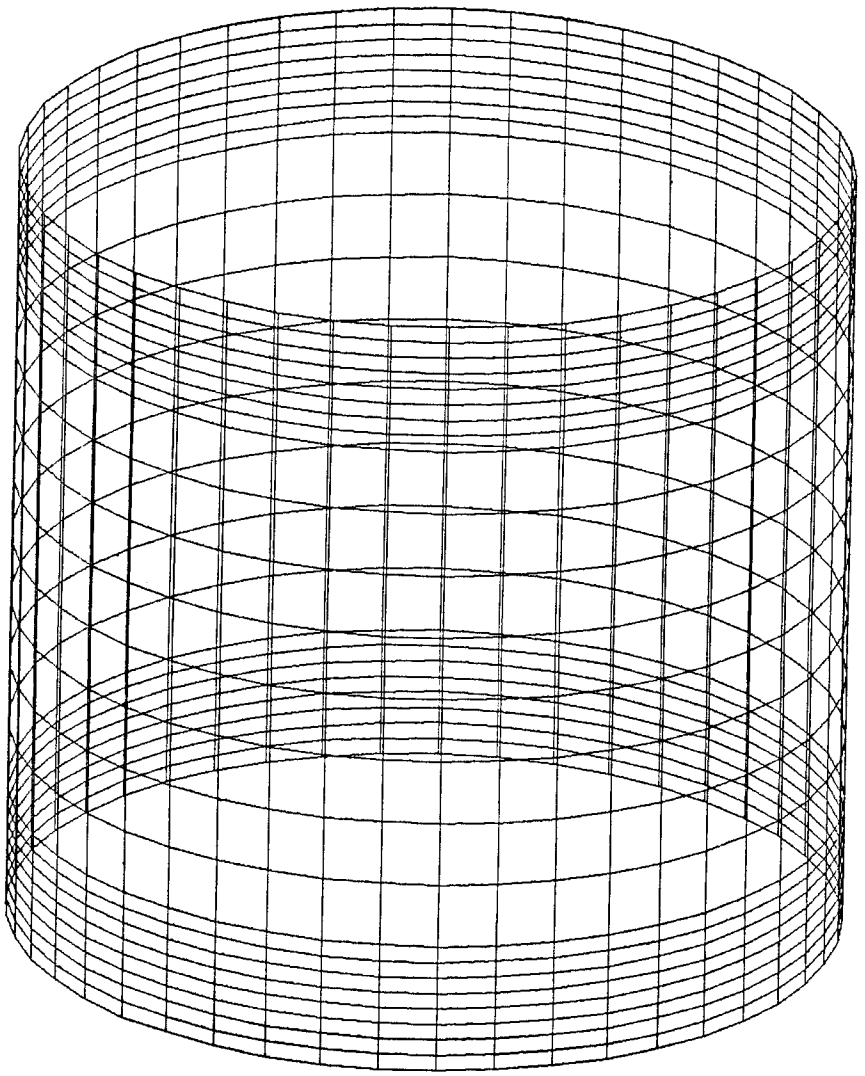

Fig. 3.1. Finite element model of TDF chamber.

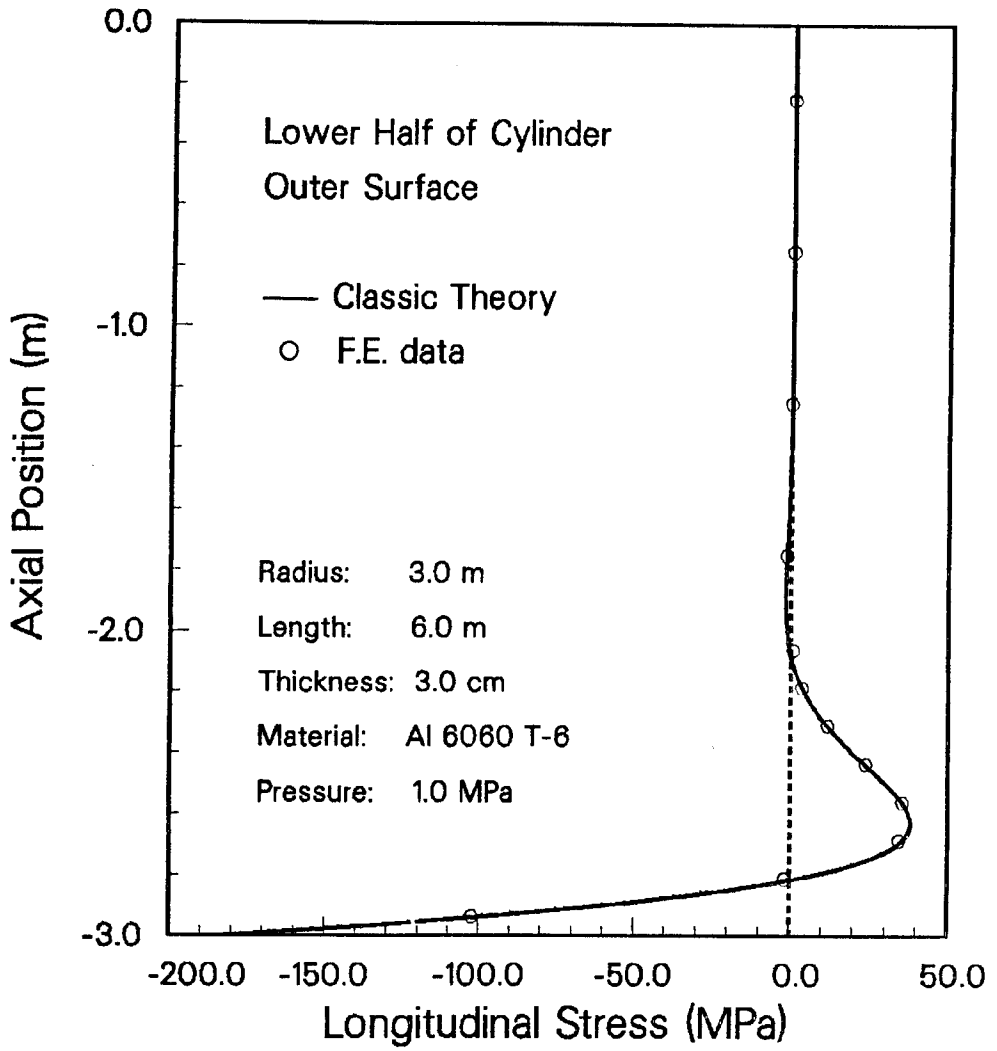

Fig. 3.2. Comparison of finite element results with exact solution.

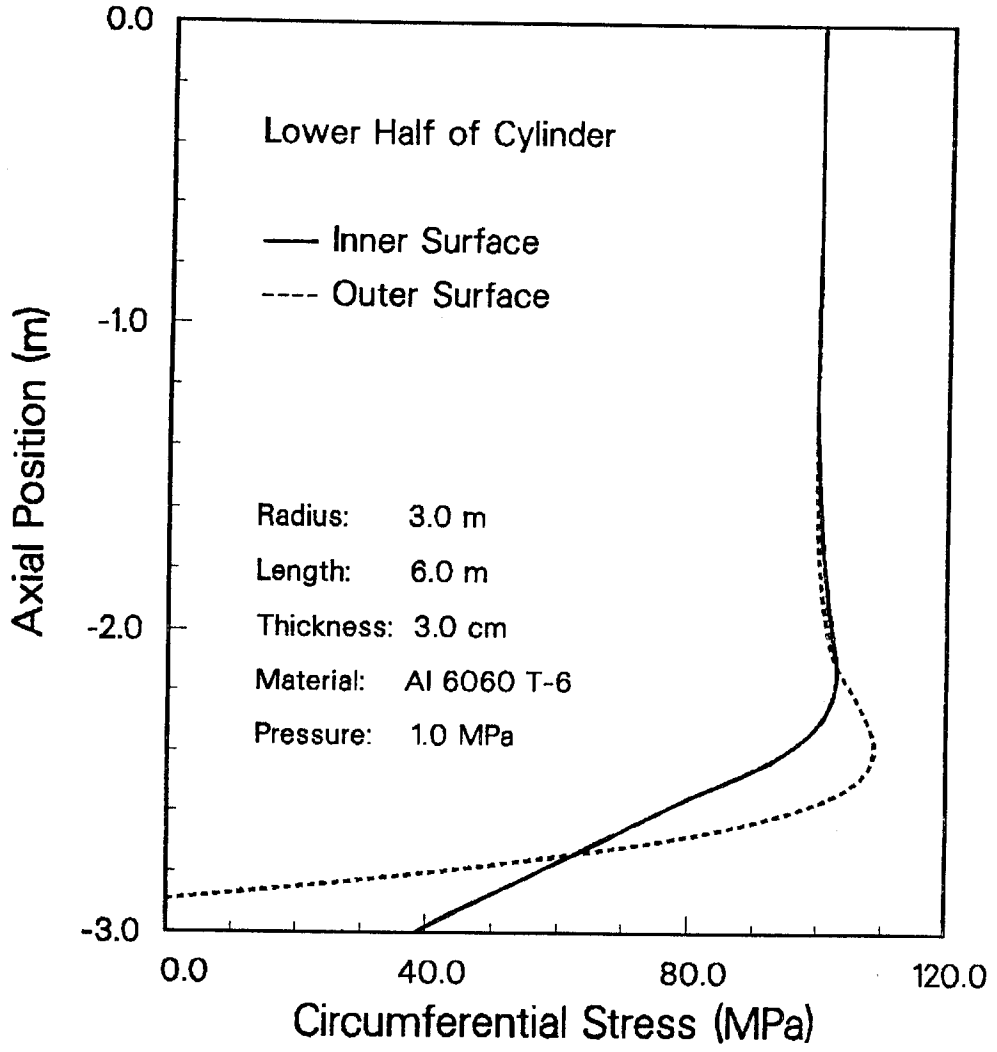

Fig. 3.3. Finite element results for circumferential stress.

Finite element computations were also used to determine corresponding displacements of the chamber. The deformed midsurface is shown in Fig. 3.4. The end circles coincide with the original size. Grids are superimposed in Fig. 3.5. Here the necessary zero end slopes and small axial displacement field can be seen. Although an exact solution for displacements can also be developed, such a comparison was not made. The precise finite element results for stresses ensures even better values for displacements since flexural stresses are essentially related to displacement gradients.

3.4. Finite Element Analysis of Beam Ports

Beam ports with a diameter of 10 cm are located at mid-height on the cylindrical vessel. Previous results showed that the principal stress in the unperforated shell was uniform, having a magnitude of 100 MPa. A square panel, 70 cm x 70 cm, with a 10 cm central hole was isolated and loaded by a uniform edge stress of 100 MPa. Because of symmetry, only one quarter of this unit was analyzed as shown in Fig. 3.6. Each quadrant consisted of eighty elements.

Finite element stress results are shown in Fig. 3.7. The largest normal stress is tangent to the beam port, in the circumferential direction, having a magnitude of 299.6 MPa, i.e., a stress concentration factor of three. Profiles of secondary normal stresses are also shown, with all approaching uniform values within one diameter from the port. Along these edges, the finite element results also included some shear stress, the largest value being 9.06 MPa (3%). From symmetry considerations, such edges are free of shear stress.

The program was also used to determine the displacement field near the beam port. Results appear in Fig. 3.8. Symmetry requires the vertical and horizontal edges through the port to remain straight. Displacement components are shown relative to these reference positions.

3.5 Concluding Remarks

These results indicate that reaction chamber stresses can be obtained accurately and economically by finite element methods if grid sizes are selectively chosen to efficiently model zones with either low or high flexural gradients. Similarly, if symmetry is exploited, a moderate number of elements is sufficient to determine accurate values for the stress concentration effects produced by beam port perforations in the chamber wall. In the detailed chamber design both of these high local stresses can be controlled by appropriate reinforcing rings.

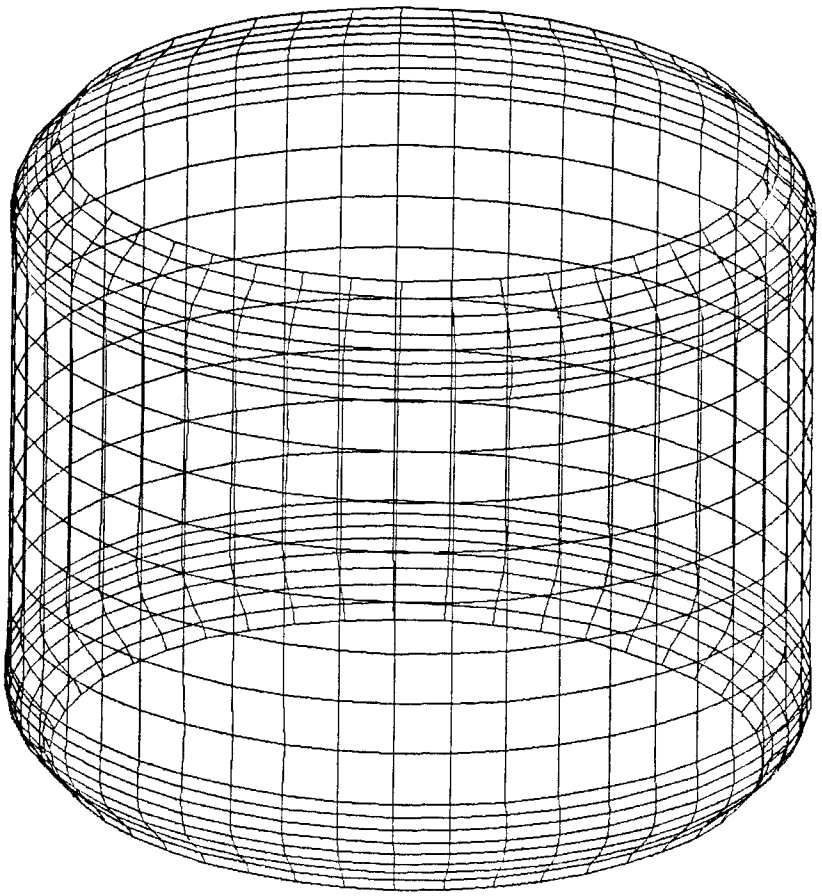

Fig. 3.4. Deformed TDF chamber.

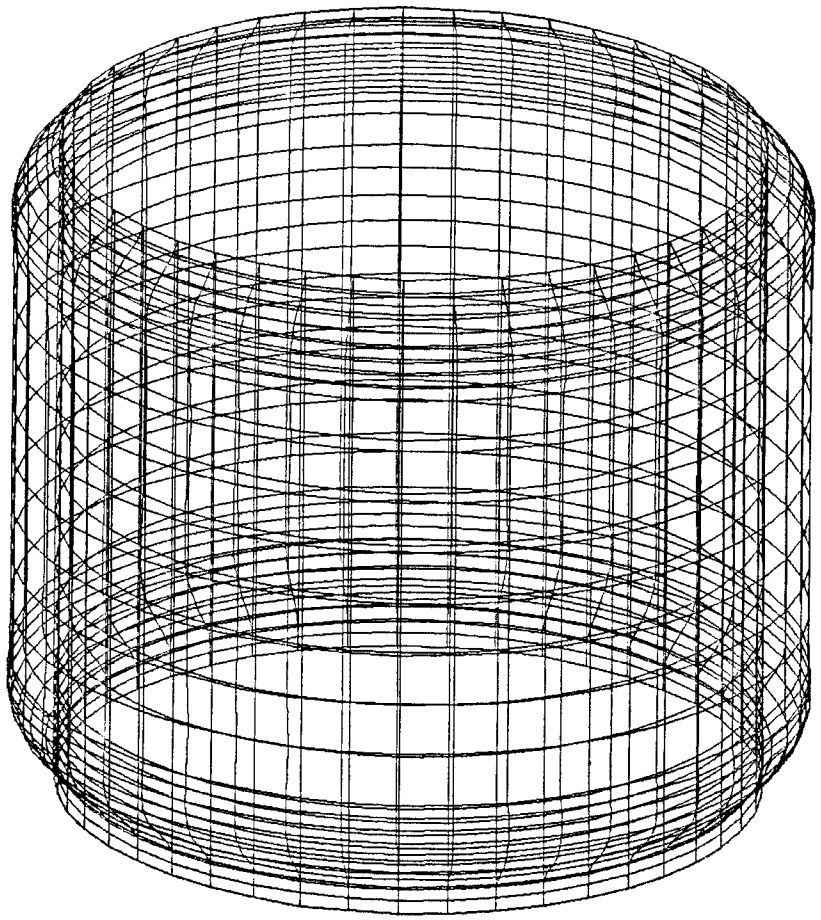

Fig. 3.5. Displacements superimposed on chamber model.

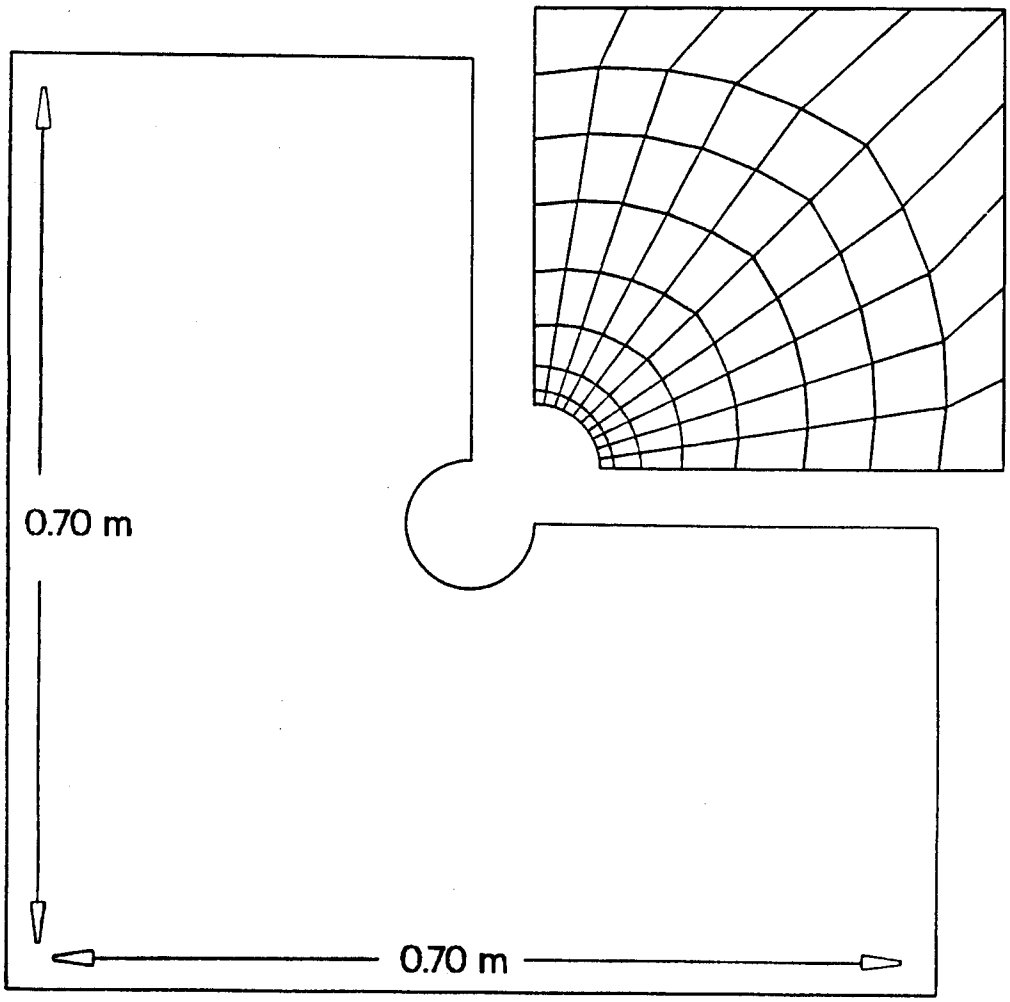

Fig. 3.6. Finite element model of beam port region.

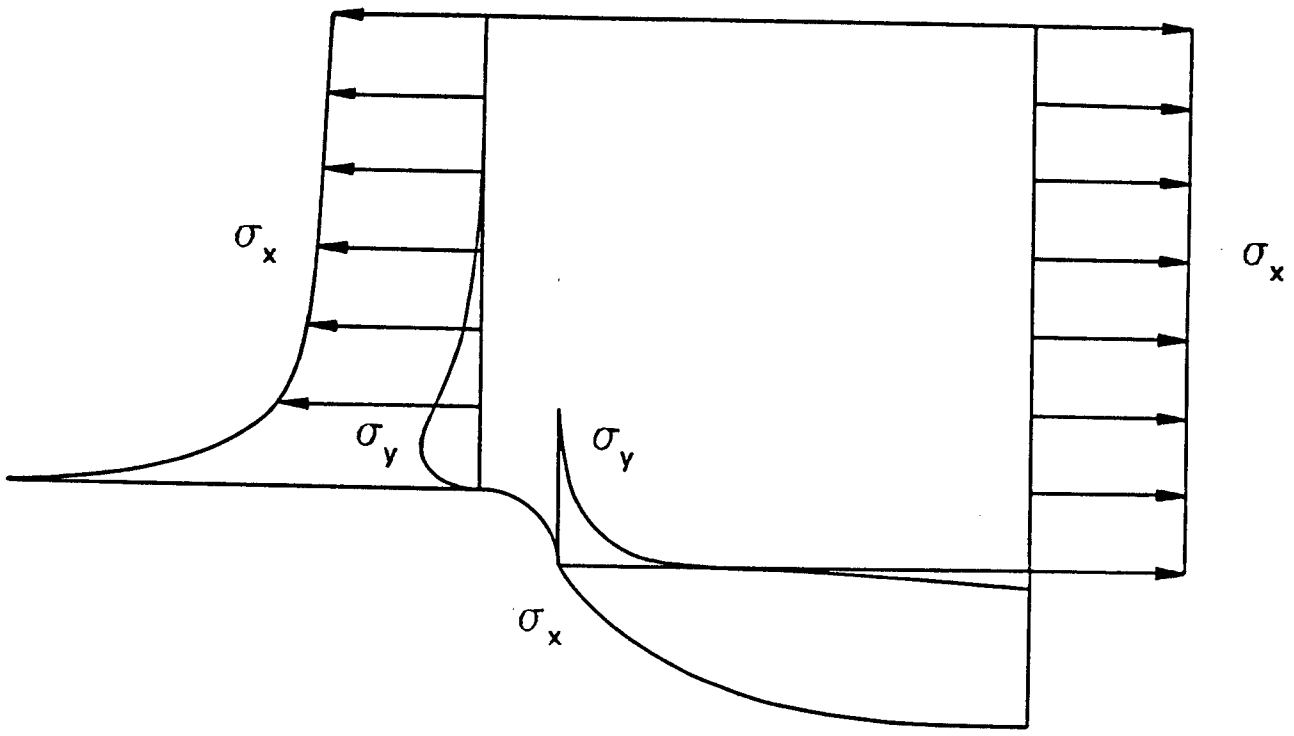

Fig. 3.7. Finite element stress distributions.

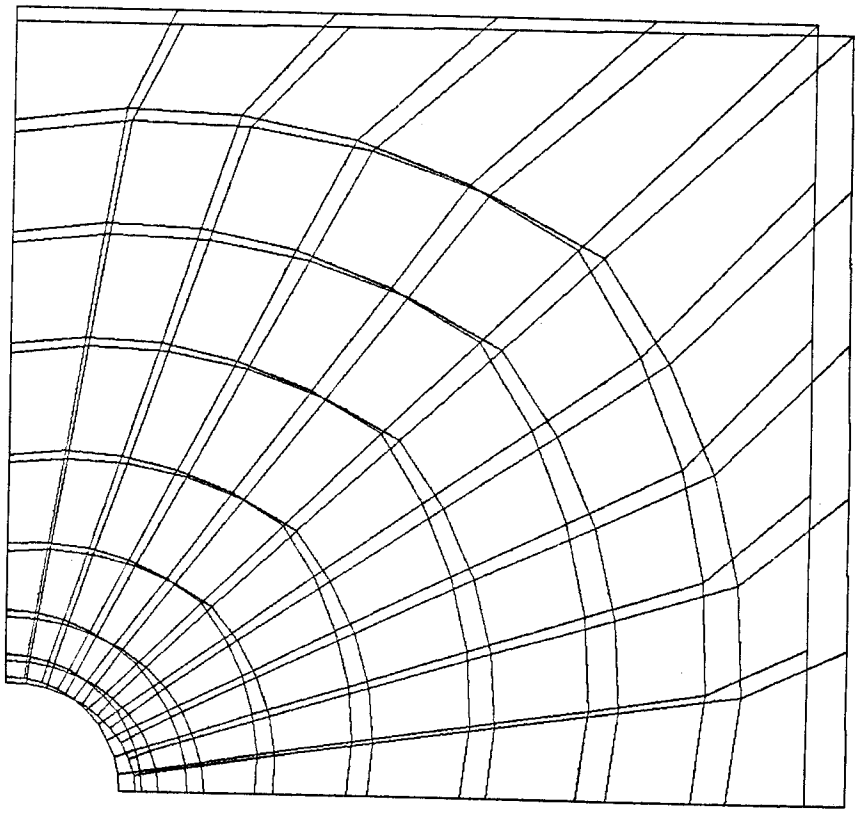

Fig. 3.8. Displacement field near beam port.

4. PLASMA CHANNEL FORMATION

Plasma channels must be formed with an azimuthal magnetic field having the proper magnitude and spatial profile if the light ion beams are to propagate from the diodes to the target with a high efficiency. Parameters for the beam ions are listed in Table 4.1. Nominal parameters for the plasma channels that are required to allow a high efficiency of propagation are shown in Table 4.2.

Table 4.1. Ion Beam Parameters

Propagation Length (m)	3
Focal Spot Radius at Target (cm)	0.5
Ion Species	Li
Nominal Ion Energy (MeV)	30
Maximum Angle Between Ion Trajectory and Channel (radians)	0.10 - 0.15
Focal Spot Radius at Channel Entrance (cm)	0.35

Table 4.2. Nominal Plasma Channel Parameters

Channel Length (m)	3
Channel Radius (cm)	0.5
Azimuthal Magnetic Field at Channel Radius (kG)	28
Background Gas Species	Nitrogen
Background Gas Density (g/cm^3)	2×10^{-5}

The ZPINCH computer code[1] was used to study the formation of plasma channels with the characteristics described above. This is a one-dimensional Lagrangian magnetohydrodynamics computer code in cylindrical geometry with radiant and conductive heat tranfer. Radiant heat transfer is calculated in a diffusion approximation, where the radiation spectrum is divided into 20 energy groups. The code allows the user to either provide parameters for the external circuit that drives the discharge current, or to just stipulate the discharge as a function of time. The second option has been used with discharge current histories constructed of two pulses, as shown in Fig. 4.1. The current history is similar to that used by Freeman, Baker, and Cook[2], in calculations that were reported several years ago. Our approach has been to modify this current history to optimize the magnetic field at the edge of the channel. This history was varied by changing the time delay, Δt, of the second pulse. The initial conditions of the

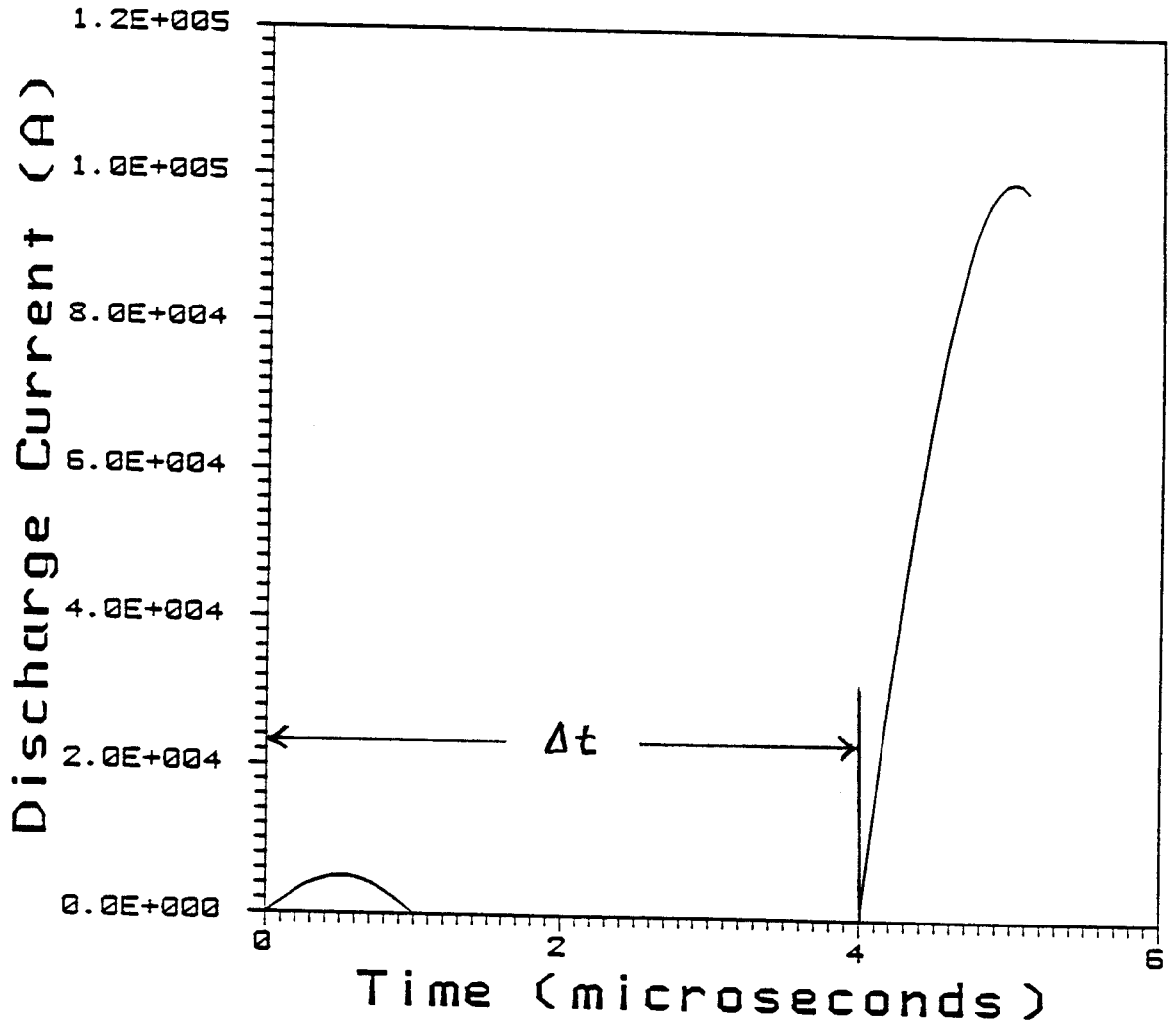

Fig. 4.1. Discharge current history. Δt is the time delay.

channel plasma were also varied. The channel plasma was pre-ionized with a laser that has a Gaussian profile. The plasma has an initial temperature profile that is also Gaussian, characterized by the half-width, λ, which is shown in Fig. 4.2. By varying these two parameters, the matrix of calculations shown in Table 4.3 was performed.

Table 4.3. Matrix of ZPINCH Calculations

	Time Delay (μs)				
Laser Radius (mm)	1	2	3	4	5
1	X	X			
2	X				
3	X	X			
4	X				
5	X	X	X	X	X

Stipulating the discharge current history neglects the problems faced in creating the discharge current. The inductance of the channel is high enough that large voltages are required to achieve a rise time of one μs. For six meter long channels (three meter channel and three meter return current path), the inductance is about six μH, if one assumes the permeability of free space. For the current history shown in Fig. 4.1, this leads to discharge voltages of 600 kV, which could easily lead to breakdown between the channel and target chamber structures. Our approach has been to find the current histories that provide acceptable channels, and then to address these problems in creating them. The opposite approach was taken in the past[3], with the result that no reasonable magnetic field magnitudes were achieved for conservative discharge current histories.

Results are summarized in Figs. 4.3 and 4.4. Fig. 4.3 shows the magnetic fields at 0.5 cm from the center of the channels and the maximum fields plotted against the time delay for the second pulse and a laser width of 0.5 cm. In these calculations, radiant energy transport has been neglected. In Fig. 4.4, these fields are plotted against the laser radius for a time delay of one μs. Here, the calculations are done with and without radiant heat transfer. One can see that generally the field at 0.5 cm from the channel axis increases as the time delay and the laser radius are decreased. Also, the field is reduced if one allows for radiant heat transfer in the calculation.

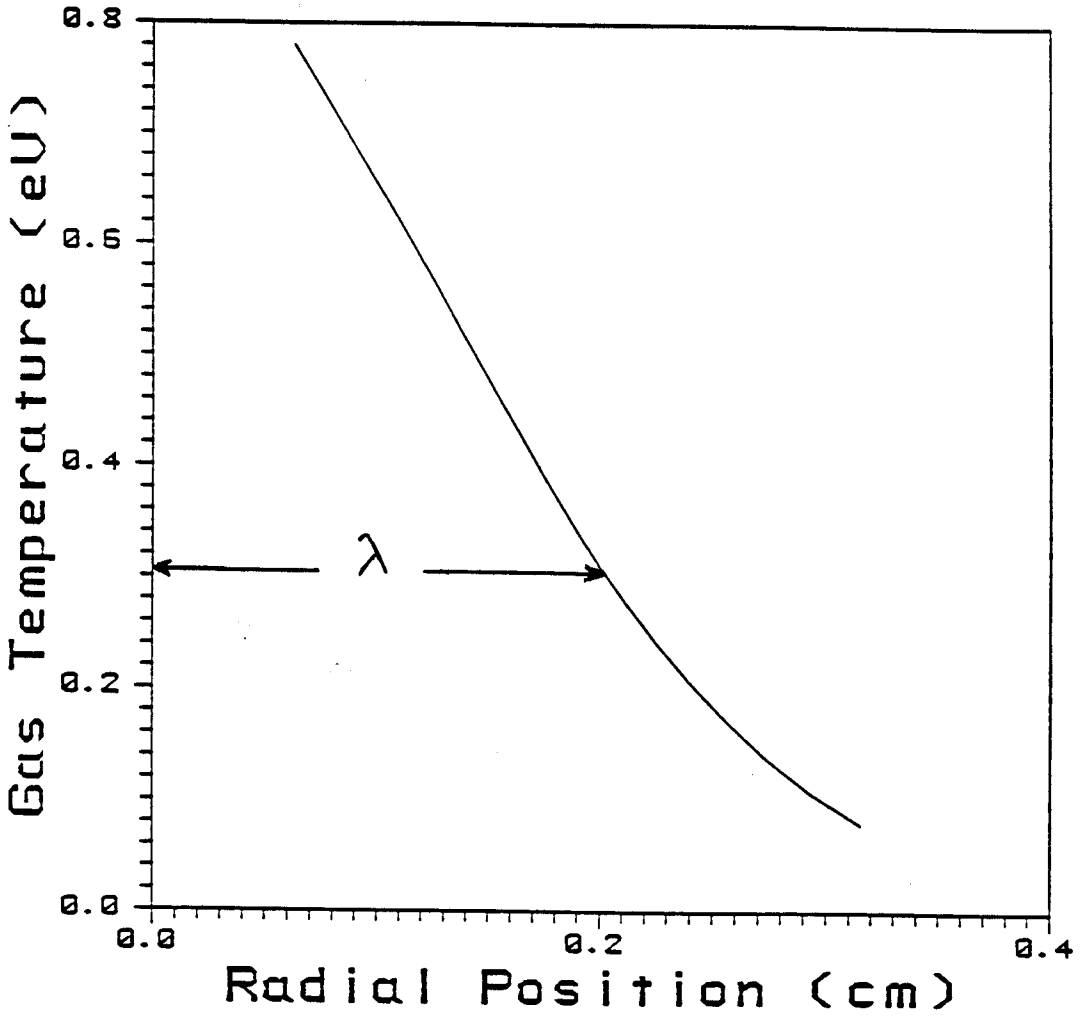

Fig. 4.2. Initial gas temperature profile. λ is the Gaussian width of the laser.

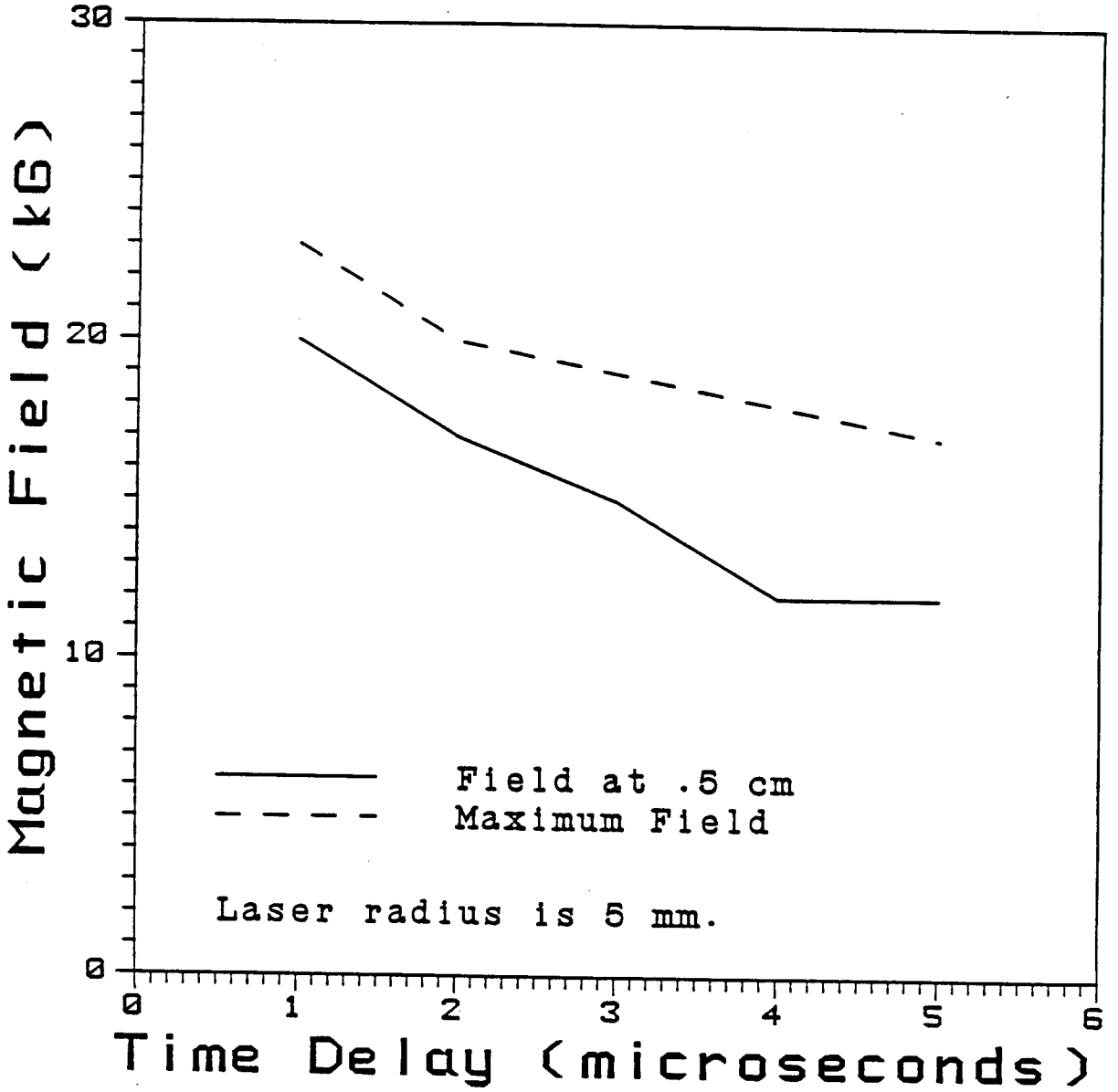

Fig. 4.3. Magnetic fields at 0.5 cm from the center of the channels and the maximum fields plotted against the time delay for the second pulse for a laser width of 0.5 cm.

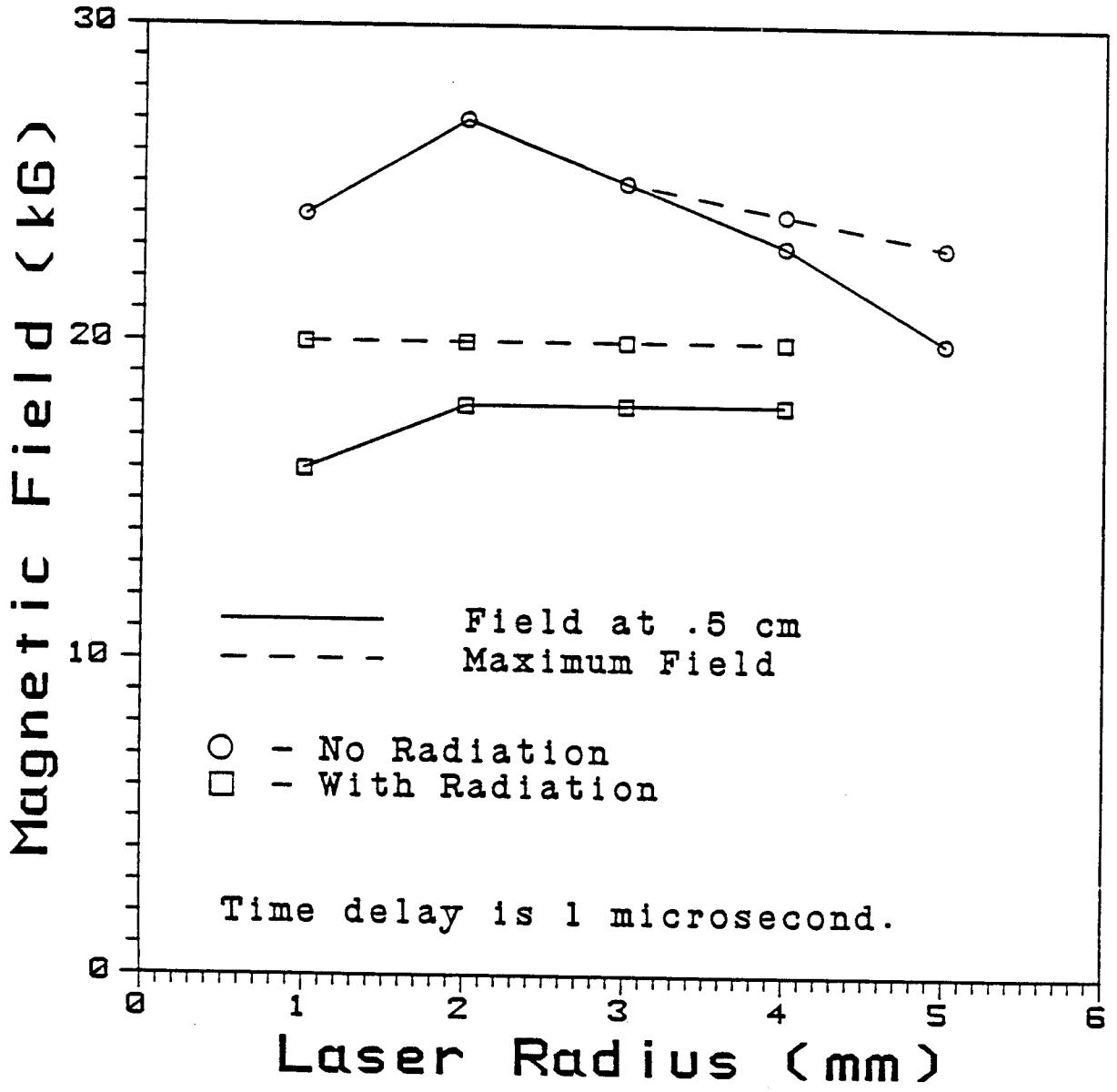

Fig. 4.4. Magnetic fields at 0.5 cm from the center of the channels and the maximum fields plotted against the laser radius for a time delay of 1 microsecond. Here, we have done calculations with and without radiant heat transfer.

The key to understanding these results is in the radial profile of discharge current. Only that part of the discharge current that flows within 0.5 cm of the channel axis contributes to the azimuthal magnetic field at 0.5 cm. The discharge current profile is dictated by the radial resistivity profile. The resistivity of the channel plasma is a strong function of temperature, so the discharge current profile is determined by the plasma temperature profile. For nitrogen, when the temperature is below about one eV, the resistivity is about 3×10^{5} ohm-m, while above this temperature the resistivity very rapidly falls to 10^{-4} ohm-m. With this explanation in mind, one can understand why a decrease in Δt should lead to a higher magnetic field at 0.5 cm. For a longer time delay between pulses more time is available for the plasma temperature to diffuse before the maximum discharge current is reached. Similarly, for a narrower initial temperature profile the field at 0.5 cm is higher because the temperature profile can radially diffuse more before current flows at radial positions greater than 0.5 cm. Also, one can imagine how radiation could spread the region of hot plasma and thus degrade the channel performance.

As an example, details of the "best" channel calculations are presented. The highest magnetic field at 0.5 cm radius is achieved when the time delay is one microsecond and the laser width is two mm. For a calculation where radiation is neglected, plasma temperature, resistivity, and mass density profiles at various times, and Lagrangian zone boundaries versus time are shown in Fig. 4.5. In Fig. 4.6 the magnetic field profile at the same times as in Fig. 4.5 is given. Figures 4.7 and 4.8 display the same quantities for a calculation where radiation is not neglected. When radiation is not considered, one sees in Fig. 4.5 that the region of hot plasma does not spread out much beyond 0.5 cm and similarly for the region of low resistivity. Therefore, in Fig. 4.6, the maximum field is near 0.5 cm and has a maximum value of 27 kG, close to the required value. One also sees in Fig. 4.5 that the channel tries to pinch when the large second pulse starts at one microsecond, but that the high temperature, and therefore high pressure, in the center of the channel stagnates the pinch so the mass density in the channel center remains low. When radiation is considered, one sees in Fig 4.7 that the high temperature and low resistivity regions do spread out to about a one cm radius, so the magnetic field in Fig. 4.8 has a maximum at about a one cm radius and the field at 0.5 cm is only about 16 kG. Also, Fig. 4.7 shows that the pinch does not stagnate until the mass density reaches an unacceptably high value because the temperature in the channel center is reduced by radiation.

From these channel calculations it has become evident that radiation heat transfer plays an important role in channel physics. The radiation diffusion model currently used in ZPINCH predicts that radiative heat transfer plays a dominant role. Blast wave simulations of small scale laser experiments using the same radiation diffusion model indicate that it overpredicts radiant heat fluxes.[4] If this is the case for channel calculations, the true result will be bounded by the calculations presented here.

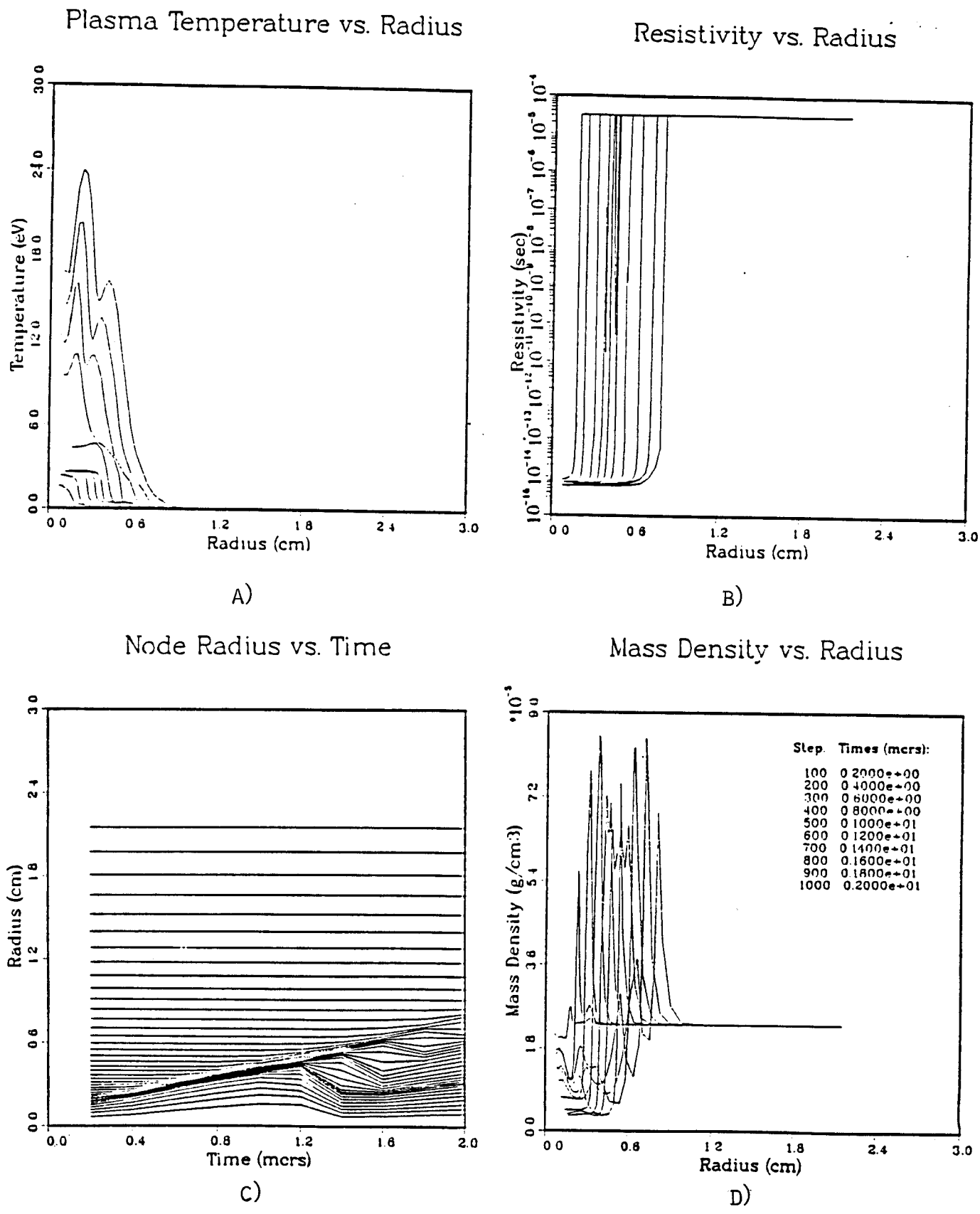

Fig. 4.5. "Best" channel simulation where radiative heat transfer has been neglected. a) plasma temperature versus radius for various times. b) plasma resistivity versus radius for various times. c) Lagrangian zone boundaries versus time. d) plasma mass density versus radius for various times.

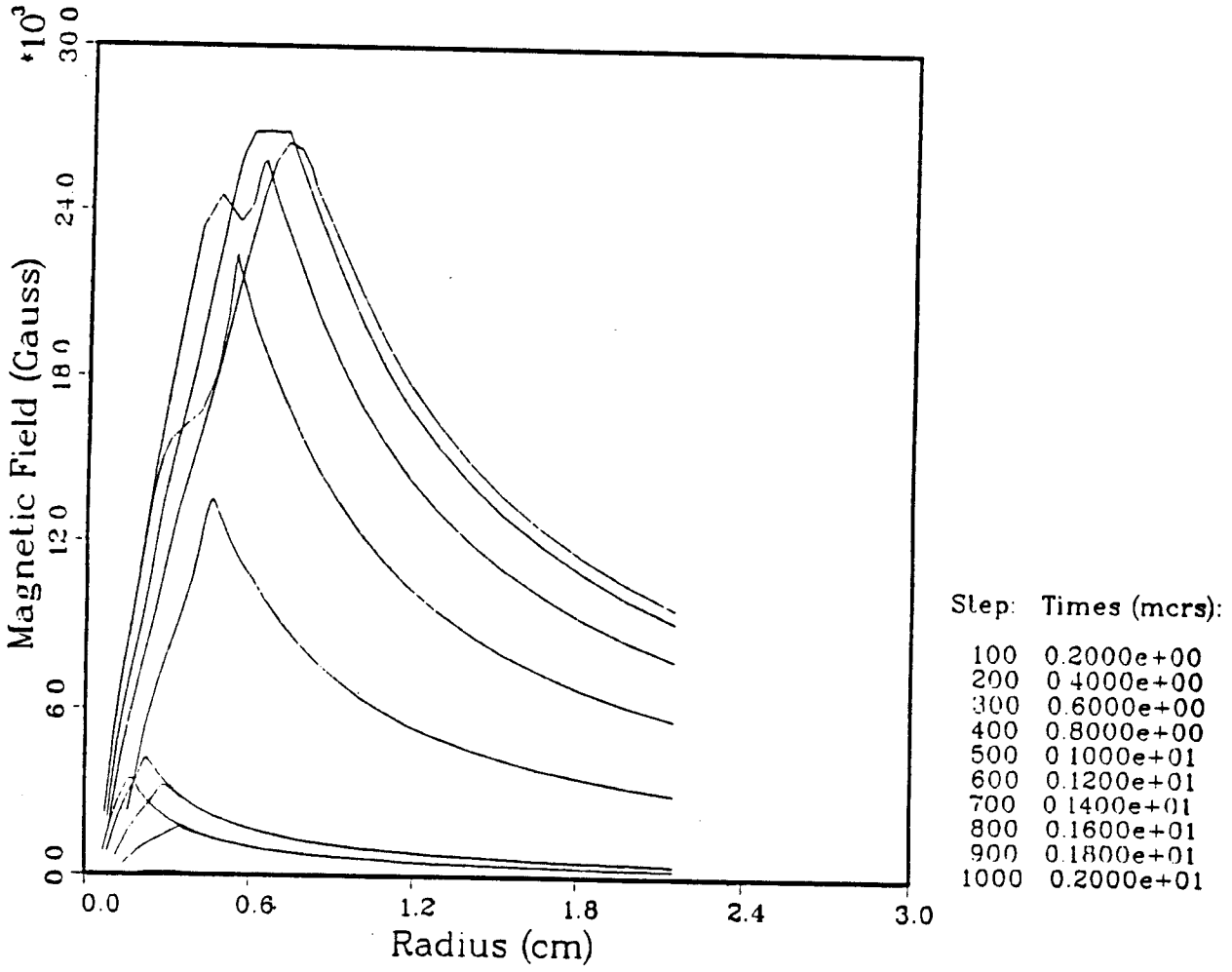

Fig. 4.6. Magnetic fields for the "best" channel simulation where radiative heat transfer has been neglected.

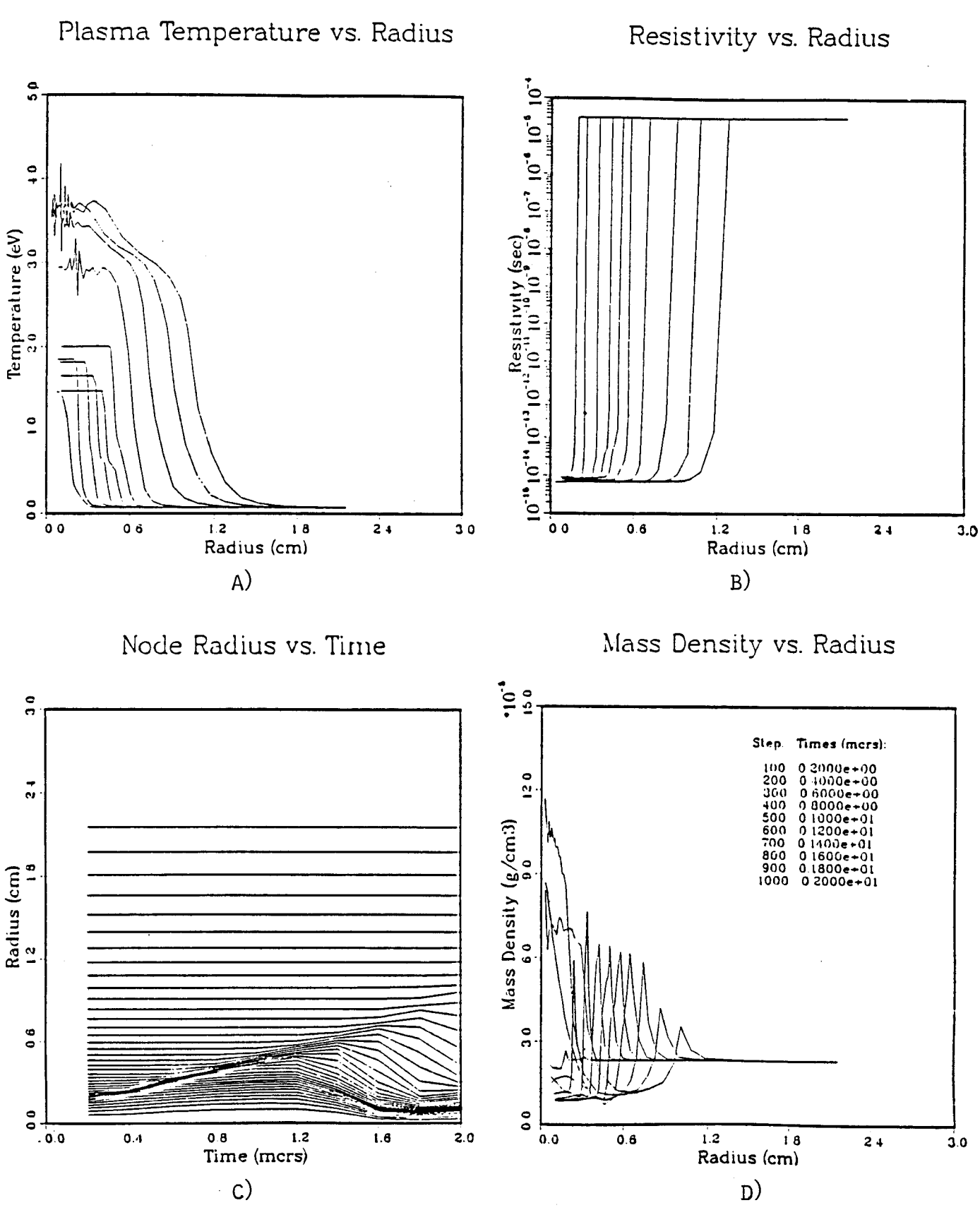

Fig. 4.7. "Best" channel simulation where radiative heat transfer has been included. a) plasma temperature versus radius for various times. b) plasma resistivity versus radius for various times. c) Lagrangian zone boundaries versus time. d) plasma mass density versus radius for various times.

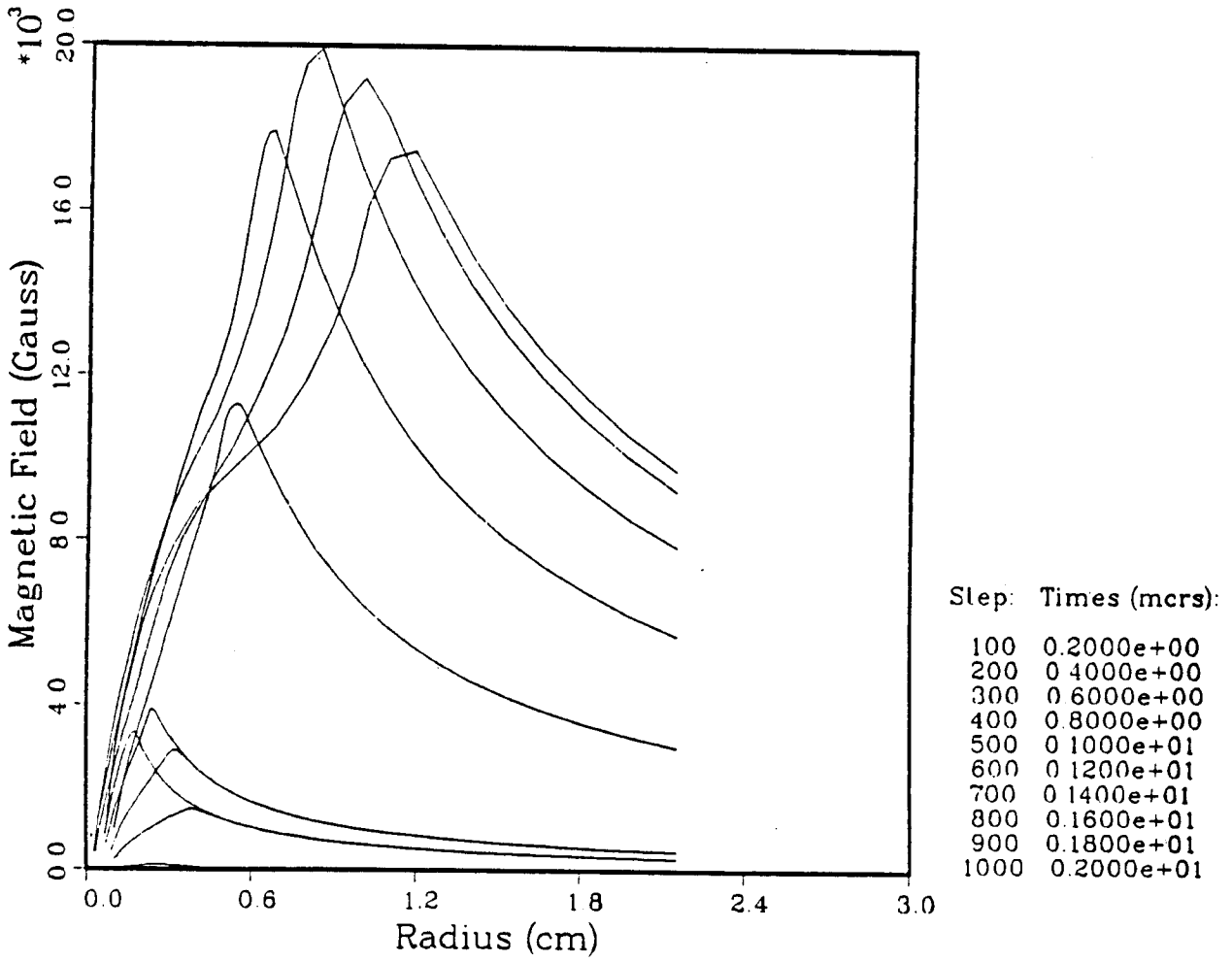

Fig. 4.8. Magnetic fields for the "best" channel simulation where radiative heat transfer has been included.

References for Section 4

1. J.J. Watrous, G.A. Moses, and R.R. Peterson, "ZPINCH - A Multifrequency Radiative Transfer Magnetohydrodynamics Computer Code," University of Wisconsin Fusion Technology Institute Report UWDFM-584 (revised June 1987).

2. J.R. Freeman, L. Baker, and D.L. Cook, "Plasma Channels for Intense Light Ion Beam Reactors," Nucl. Fusion 22, 383 (1982).

3. R.R. Peterson, G.A. Moses, J.J. Watrous, and R.E. Olson, "Plasma Channels for Light Ion Beam Propagation in the Target Development Facility," University of Wisconsin Fusion Technology Institute Report UWFDM-666 (November 1985).

4. J.J. MacFarlane, G.A. Moses, and R.R. Peterson, "Energy Deposition and Shock Wave Evolution from Laser-Generated Plasma Expansions," University of Wisconsin Fusion Technology Institute Report UWDFM-723 (May 1987).

5. ION BEAM OVERLAP ON THE TARGET

The TDF will use discharge plasma channels to guide the ion beams from the ion diodes to the target. In the current TDF concept, 12 plasma channels carry the ion beams. The plasma channels function by providing a strong azimuthal magnetic field that keeps the ions close to the axis of each channel. As the plasma channels converge on the target, the azimuthal magnetic fields from adjacent channels destructively interfere with each other and no longer confine the ions. If the fields begin to interfere far enough away from the target, then a significant number of ions will miss the target. The ION particle tracking computer code has been used to study this issue in the TDF.

The ION code[1] calculates the trajectories of ions in an arbitrary magnetic field. The user defines a source of ions with a prescribed distribution of initial positions and initial directions. The code randomly chooses ion initial directions and positions from this source and calculates their trajectories in the presence of an arbitrary magnetic field. The source of ions may be instantaneous or it may have a finite current that is a function of time. The energies of the ions may be constant or may be functions of the time the ions are released from the source. The energy of each ion is assumed to remain constant throughout its flight, though ion energy loss could be easily included if it is an important effect. The code uses the DGEAR package in the IMSL library to calculate the ion trajectories. This is a standard differential equation solver that uses any one of several variations of the predictor-corrector method.

The channel magnetic fields are modelled both in the overlap region and in the free-standing region far from the target. In the free-standing region, the magnetic fields are assumed to be azimuthal and independent of the position along the axis of the channel. In the overlap region, the magnetic fields are assumed to fall linearly to zero over a distance of one centimeter. The discharge current is radially uniform out to the channel radius, where it drops to zero. The radial magnetic field profile is therefore linearly increasing out to the channel radius and drops as the inverse of the radius beyond the channel radius.

In the TDF, the channels are roughly three meters long. There are 12 channels carrying ion beams and 12 return current channels. The return current channels meet the target in a cone above the equatorial plane of the target, making a large enough angle with this plane that these channels do not interfere with the ion carrying channels. In the following calculations the ion carrying channels are assumed to be 0.5 cm in radius and the magnetic field at the edge of the channels is 28 kG in the free-standing region. This corresponds to a uniform discharge current of 70 kA per channel. As the discussion in Chapter 4 indicates, a channel has yet to be designed with such parameters. The ion

carrying channels enter the target chamber in six stacked groups of two, but they may meet the target either in a single layer on the equatorial plane or in two layers. We have considered both options.

The results of ion trajectory calculations, completed with the ION code, are shown in Figs. 5.1 and 5.2. Both figures show how the fraction of ions striking the target varies with the distance from the end of the channel to the target and the maximum entrance angle for ions entering the plasma channels. The maximum entrance angle is approximately equal to R/F, where R is the outer radius of the ion diode and F is the diode's focal length. In these calculations, the ions focus onto a spot 0.35 cm in radius, which is consistent with a diode microdivergence of 0.005 radians. The end of the channel is defined as the point at which the magnetic field begins to drop below the free-standing value. In Fig. 5.1 the fraction of ions striking the target is plotted against the distance from the end of the channel for R/F ranging from 0.1 to 0.15. The vertical lines correspond to the distances between the surface of the target and the end of the channel for 12 channels meeting the target in one layer and in two layers. In Fig. 5.2 these same results are plotted in a different way: the dependence of the fraction of ions reaching the target on R/F is shown for overlap standoff distances of 0.45 cm and 1.41 cm, corresponding to two and one layers respectively. From both of these figures, one sees that the fraction of ions reaching the target decreases as R/F increases. For overlap standoff distances of 0.45 and 1.41 cm, the fraction of ions reaching the target surface is between 0.7 and 0.8.

The assumption that the magnetic fields remain axisymmetric as they decay in the overlap region is probably conservative. In the single layer geometry, the fields above and below the channels should not be reduced by interference to the same degree as the fields on the side of the channels. This means that ions whose motion is in a vertical plane would not be lost to the same degree that our calculations predict. More accurate calculations that account for this effect would require the field geometries in the overlap region. This requires knowledge of the electron discharge currents in that region, which we have no means of calculating. Perhaps a 2 or 3-dimensional particle-in-cell computer program, like those used at SNL could do such a calculation.

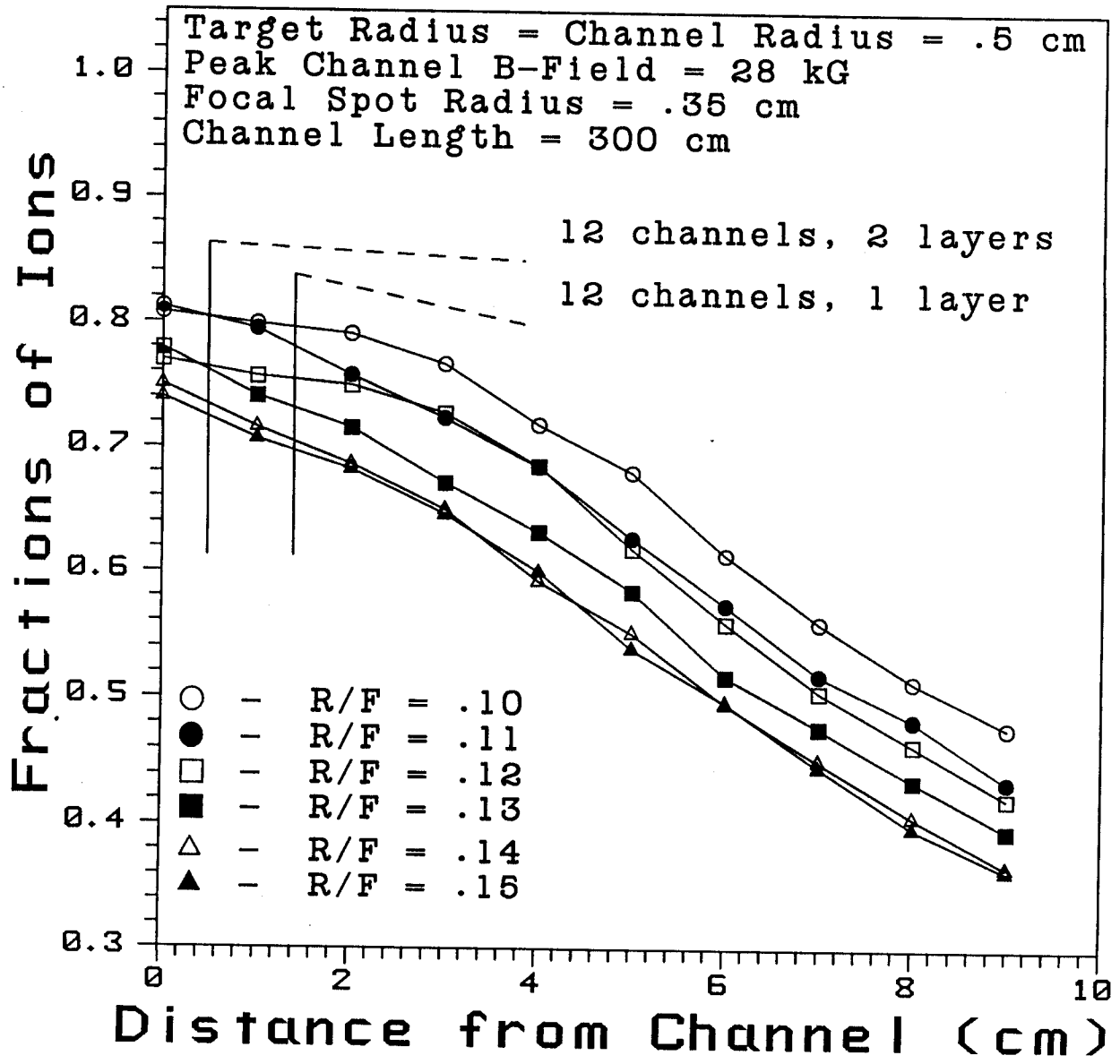

Fig. 5.1. Fraction of ions reaching target versus distance from end of channel to target surface for various R/F.

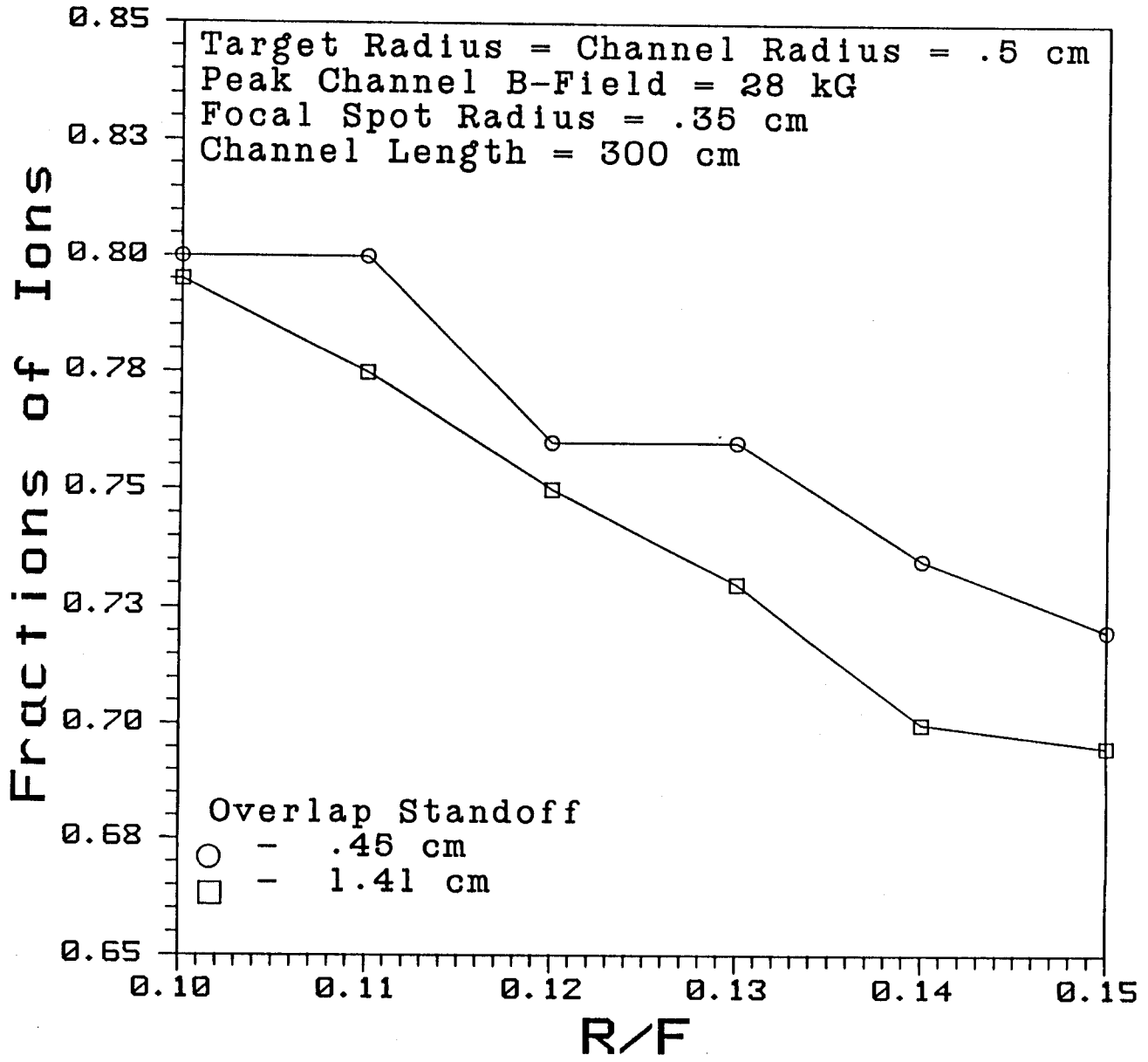

Fig. 5.2. Fraction of ions reaching target versus R/F. The distance from the end of the channel to the surface of the target is 0.45 and 1.41 cm.

References for Section 5

1. G.A. Moses, "ION - A Code to Compute Ion Trajectories in Z-Pinch Plasma Channels," University of Wisconsin Fusion Technology Institute Report UWFDM-712 (January 1987).

6. TARGET CHAMBER DESIGNS

The TDF would provide a means of testing high gain inertial confinement fusion targets at a rate of 10 shots per day[1]. The target would yield from 50 to 800 MJ of energy per explosion when it is irradiated with a collection of beams of ions containing a total of 10 MJ in a properly designed pulse. The energy released in the target explosion is about 72% in neutrons and 28% in x-rays and debris ions. The target x-rays and ions deposit their energy in the target chamber gas in a manner that generates a blast wave that mechanically and thermally loads the wall of the target chamber. The target chamber must survive these loads.

Two target chamber designs have been pursued. Each faces these issues differently. One design, shown in Fig. 6.1, attempts to minimize the induced radioactivity in the target chamber structure with the use of a graphite moderator. Under some circumstances, radioactivity due to fusion neutrons can be reduced by softening the neutron spectrum[2] and this design uses this fact. The graphite neutron moderator is roughly 50 cm thick and the target chamber has a radius of three meters. The second design is much smaller, one meter in radius, and has only a thin liner of graphite. This is shown in Fig. 6.2. In this design, ion beams and radiation for diagnostics must propagate through much less target chamber gas than in the first design. Results are presented for both designs when the first wall structural material is an aluminum alloy, although steel has also been considered.

6.1 Target Chamber Gas Behavior

The target chamber gas must be able to sustain plasma discharge channels for ion beam propagation, yet must also allow diagnostics of the target performance. The formation and behavior of plasma channels in the TDF has been simulated with the ZPINCH[3] computer code and the limits on the ion power per channel have been determined with the WINDOW computer code.[4] The issue of channel behavior and ion beam propagation is far from settled, but at this time, our best estimate is that nitrogen gas at a number density of 10^{17} cm^{-3} is adequate for plasma channel formation.[5] Some diagnostics require that few hundred eV x-rays propagate sufficiently through the gas to detectors, while others require the collection of target debris. The target chamber gas will interfere with these diagnostics to some degree, but it is still necessary to determine the maximum allowed gas density and distances between the target and the diagnostics. For the work presented in this paper, only beam propagation is used to determine the target chamber gas and 10^{17} cm^{-3} nitrogen is chosen.

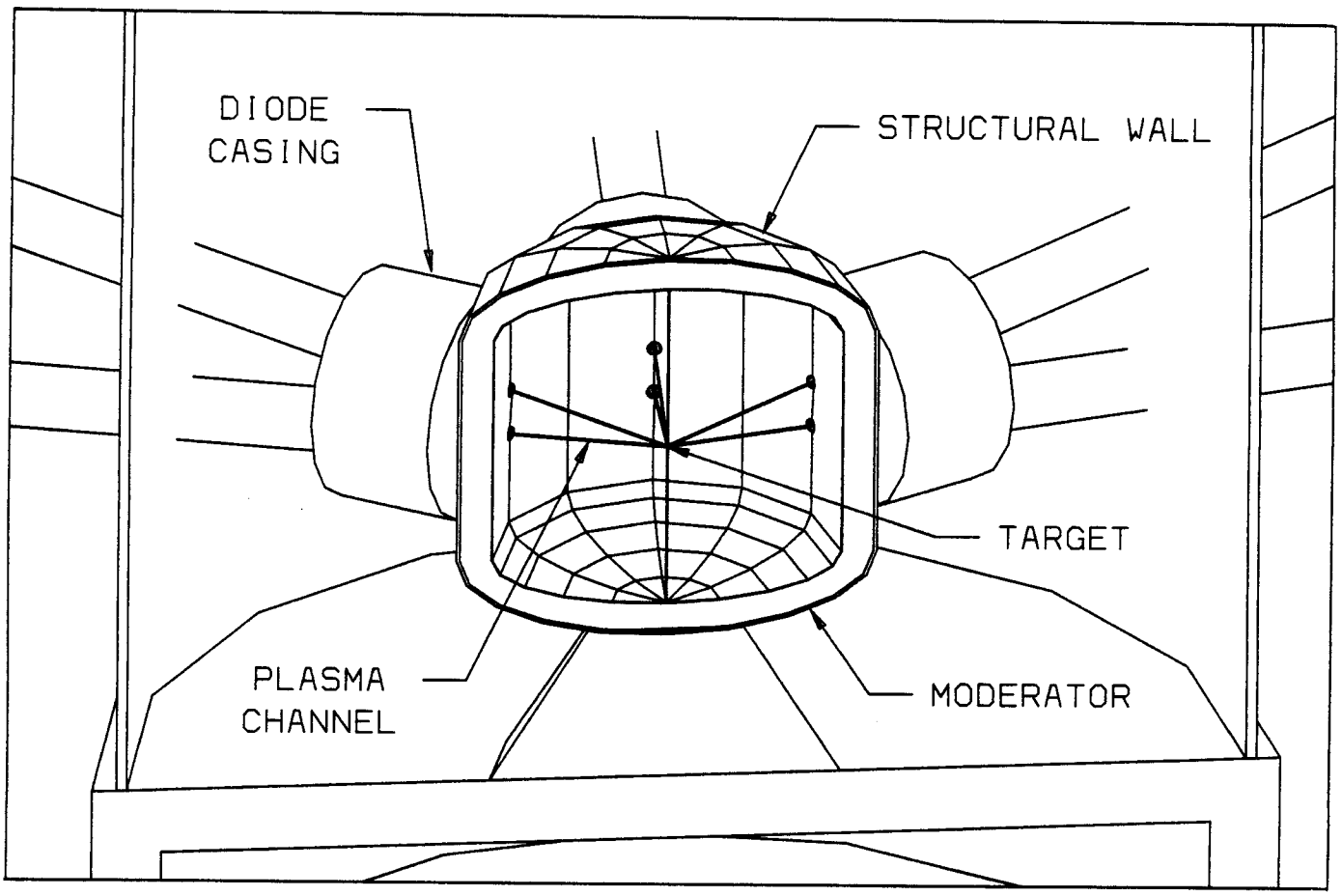

Fig. 6.1. Target chamber design with graphite neutron moderator. The distance from the target to the moderator is 2.5 m.

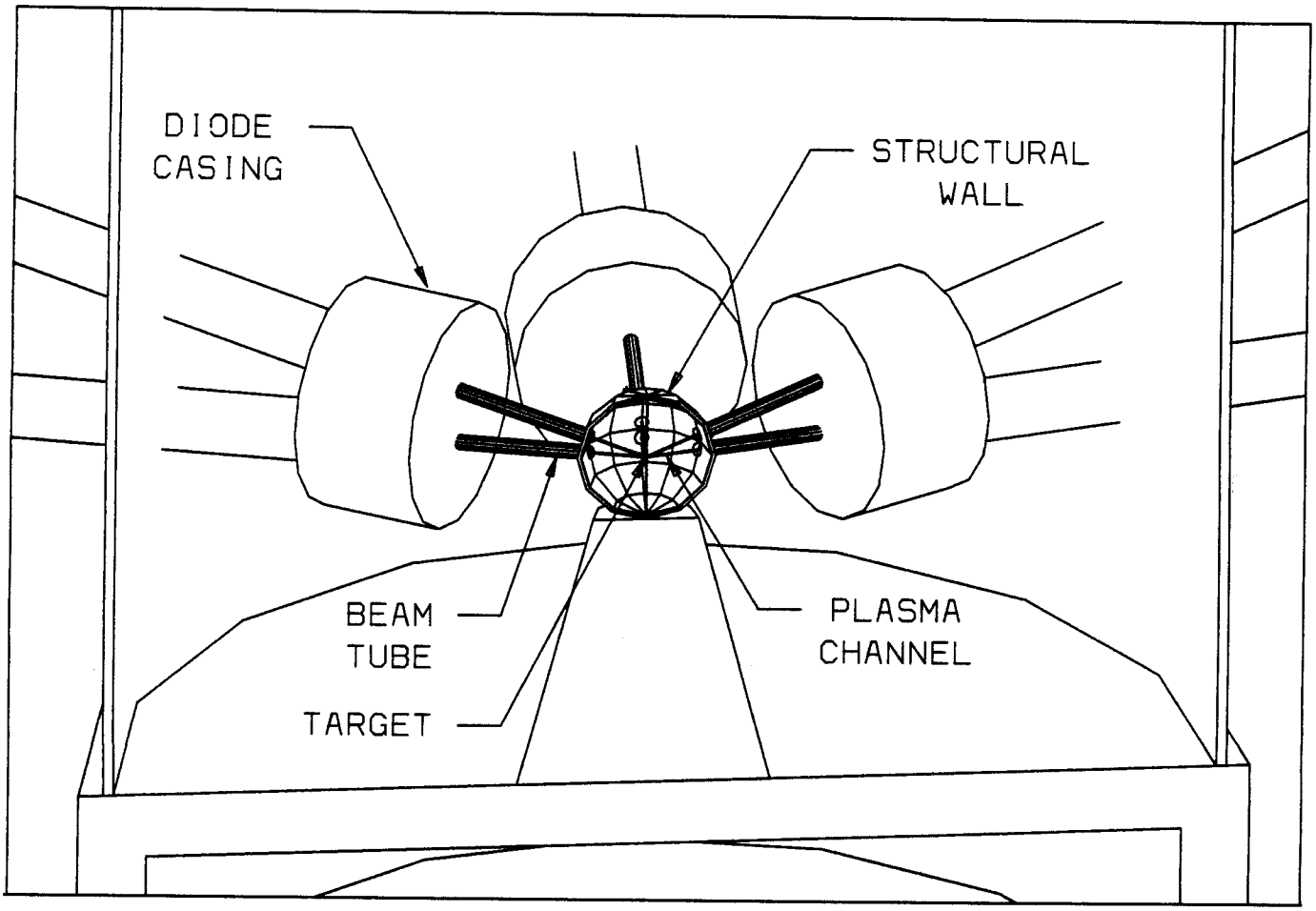

Fig. 6.2. Target chamber design without neutron moderator. The distance from the target to the first surface is 1 m.

The details of the target explosion dictate where the target yield energy deposits, and this directs the target chamber gas behavior. The main mission of the TDF is to test high yield targets so that target designs can be optimized. For this reason, the details of the target explosions will change over the lifetime of the TDF. For the purposes of this work a representative high yield target design typical of what will be used in the TDF[6] has been chosen. This target, which has a lead shell outside a shell of a lead-lithium mixture, and a hollow cryogenic deuterium-tritium fuel capsule, releases 20% of its yield in x-rays and 8% in debris ions. The typical target explosion will contain a total of 200 MJ, though the yield may range between 50 and 800 MJ. The x-ray spectrum consists mainly of a roughly one keV "blackbody" spectrum, with a much smaller component at 100 keV. Debris ions have a normalized energy of 0.85 keV/amu and include deuterium, tritium, helium, lithium and lead.

The target x-ray and ion deposition in the target chamber gas has been calculated and the resulting mechanical loadings imposed on the target chamber walls. These calculations have been done with the CONRAD computer code.[7] CONRAD is a one-dimensional Lagrangian hydrodynamics code with multigroup radiation transport. This code simulates the formation and propagation of a blast wave in the target chamber gas and predicts the gas pressure on the wall surface. The pressures on one meter and three meter radius walls are shown in Fig. 6.3. For a three meter radius, the pressure falls to insignificant values from a one MPa maximum in about 0.3 ms. On the other hand, the one meter radius chamber pressure remains high for a much longer time. This occurs because the energy deposited per unit mass in the gas is much higher in the smaller chamber. These calculations are believed to be conservative because the energy lost by blast waves due to radiation has been underestimated. Since both target chamber designs have first walls lined with graphite, radiant energy to the first walls does not pose a threat to the survival of the target chamber, and this would be true even if all of the blast wave energy were released as radiation.

6.2 Target Chamber with Graphite Moderator

In the target chamber with a graphite moderator, the 50 cm of graphite is considered to be a nonstructural assembly. We assume that the moderator has no circumferential strength to oppose the radial pressure and just transfers the load to the structural first wall. Thus, the pressure pulse loading the three meter structural wall is taken as the value calculated at the inner surface of the moderator, which is an impulse of about 100 Pa-s. We have assumed that the thermal loading does not damage the graphite.

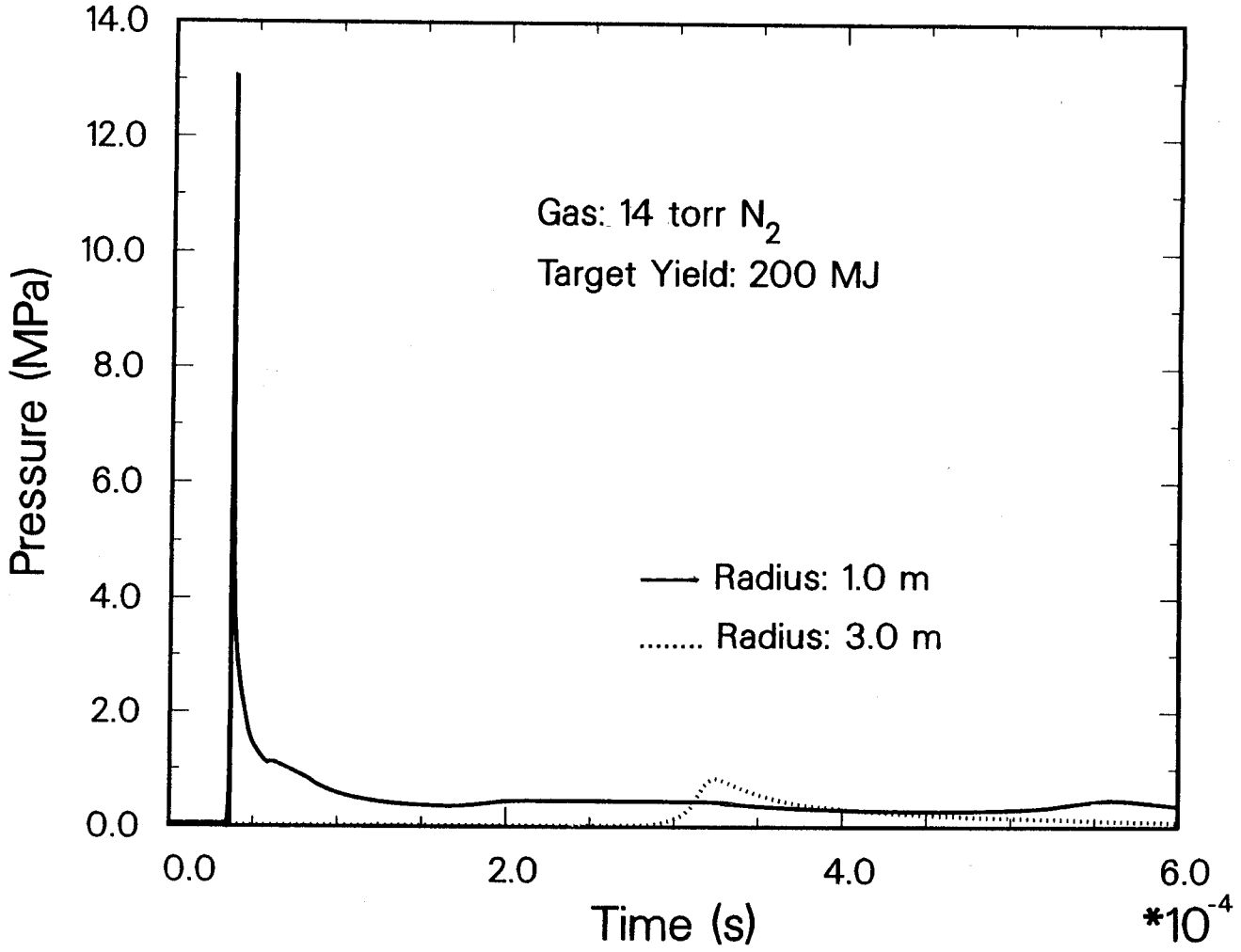

Fig. 6.3. Calculated blast overpressures on first surface of TDF versus time. Wall radii are 1 m and 3 m.

Stresses for chambers of welded 6061-T6 aluminum have been calculated. The calculated stresses would be nearly the same for 2-1/4 Cr - 1 Mo steel, though the strains in aluminum are about three times as high as in steel. The stresses are calculated with an analysis that assumes that the pressure loading occurs in an instantaneous impulse, an assumption valid when the mechanical response time is long compared with the width of the pressure pulse. The stress history for this design for a 5 cm thick wall is shown in Fig. 6.4. The peak stress of 15 MPa corresponds to a doubled strain of 7.8×10^{-4} in aluminum, which is less than the endurance limit of 8.3×10^{-4}. Therefore, the wall will survive more than the required 15,000 shots.

6.3 Target Chamber without Graphite Moderator

In the the smaller target chamber that has only a thin graphite liner, the mechanical loading is transferred directly to the structural first wall. Therefore, the pressure loading calculated at the inside surface of the graphite liner is used. The thermal loading does not damage the graphite.

One consequence of the small chamber radius is a change in the shape of the pressure pulse at the wall. The wall pressure remains significant for a much longer time than for larger chambers. Therefore, the assumption that the pressure pulse duration is short compared with the vibrational period of the wall is not valid and modal analysis cannot be used to calculate the stress histories. Instead, we have numerically solved for the wall motion and stresses, with the full time-dependent nature of the pressure loading taken into account. The pressure history for a 5 cm thick welded aluminum 6061-T6 wall is shown in Fig. 6.5. The maximum stress and doubled strain range are 12 MPa and 3.2×10^{-4}, respectively, for aluminum. The strain range is below the endurance limit and thus the chamber should sustain 15,000 shots.

References for Section 6

1. B. Badger, et al., "Light Ion Beam Fusion Target Development Facility Studies: Progress Report for the Period 1 October 1985 to 31 October 1986," University of Wisconsin Fusion Technology Institute Report UWFDM-713, October 1986.

2. D.L. Henderson, G.A. Moses, and R.R. Peterson, "Activation and Radiological Dose Calculations for the Light Ion Fusion Development Facility," J. Nucl. Mat., vol. 141-143, pp. 49-54, 1986.

3. J.J. Watrous, G.A. Moses and R.R. Peterson, "Z-PINCH - A Multifrequency Radiative Transfer Magnetohydrodynamics Computer Code," Fusion Power Associates Report FPA-85-3, 1985.

4. R.R. Peterson, "WINDOW - A Code to Compute Ion Beam Power Constraints," Fusion Power Associates Report FPA-84-6, 1984.

5. R.R. Peterson, G.A. Moses, J.J. Watrous, and R.E. Olson, "Plasma Channels for Light Ion Beam Propagation in the Target Development Facility," University of Wisconsin Fusion Technology Institute Report UWFDM-666, November 1985.

6. G.A. Moses, R.R. Peterson, M.E. Sawan, and W.F. Vogelsang, "High Gain Target Spectra and Energy Partitioning for Ion Beam Fusion Reactor Design Studies," University of Wisconsin Fusion Technology Institute Report UWFDM-396, 1980.

7. R.R. Peterson, "CONRAD - A Combined Hydrodynamics Condensation/Vaporization Computer Code," University of Wisconsin Fusion Technology Institute Report UWFDM-670, April 1986.

Acknowledgement

This work was performed for Sandia National Laboratory under contract number 32-9915. Computer support has been provided in part by the National Science Foundation at the San Diego Supercomputer Center.

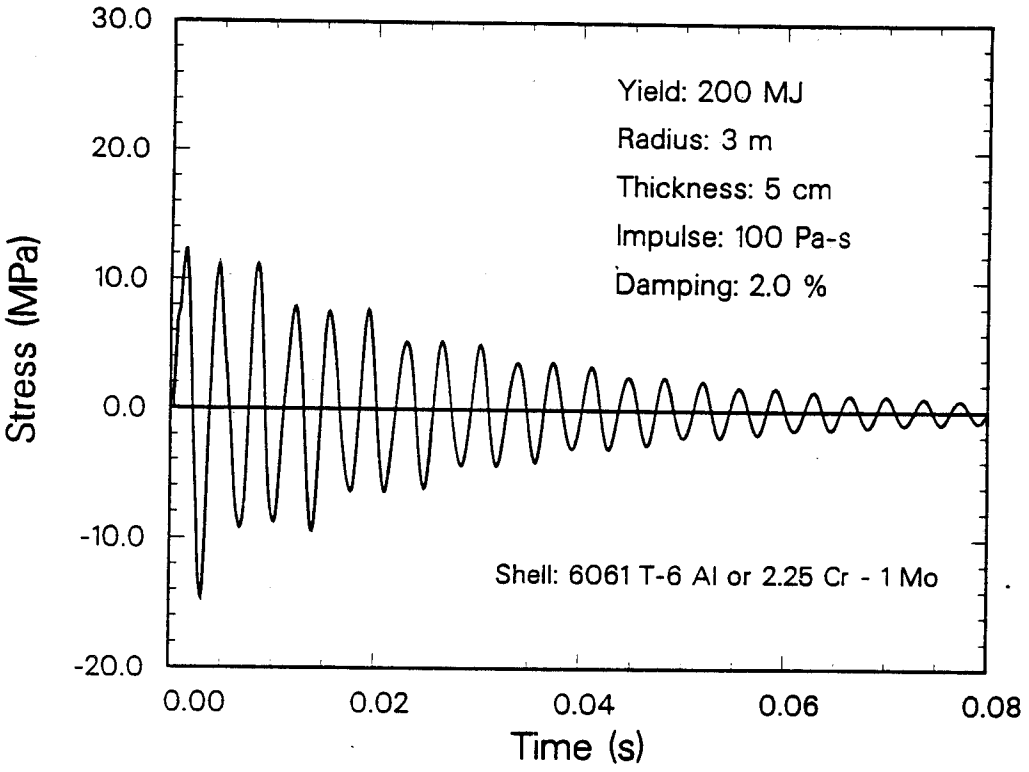

Fig. 6.4. Mechanical stresses in structural wall of target chamber design with graphite moderator.

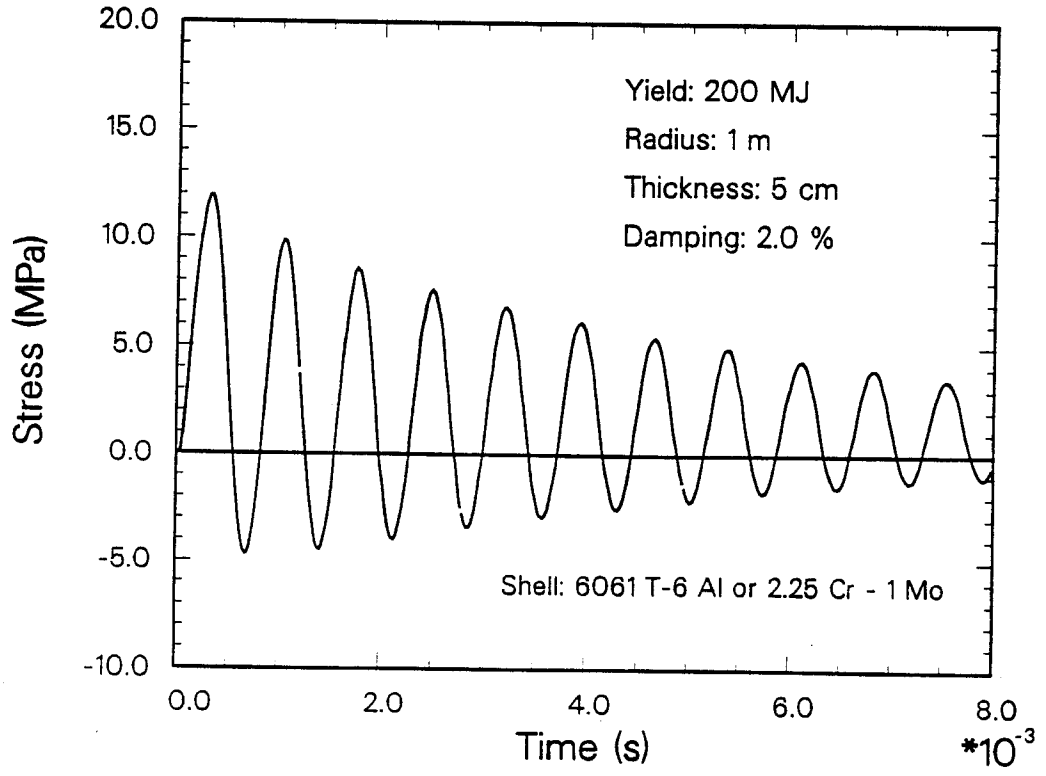

Fig. 6.5. Mechanical stresses in structural wall of TDF target chamber design without graphite moderator.